itle: Effective flow properties of heterolithic, cross-bedded tidal sandstones: Part 1. Surface-based modeling

Authors: **BENOÎT Y. G. MASSART[1,2]*, MATTHEW D. JACKSON[1], GARY J. HAMPSON[1], HOWARD D. JOHNSON[1], BERIT LEGLER[1,3], CHRISTOPHER A.-L. JACKSON[1]**
[1] Department of Earth Science and Engineering, Imperial College London, South Kensington Campus, London SW7 2AZ, UK.
[2] Current address: Statoil ASA, Sandsliveien 90, Bergen 5254, Norway.
[3] Current address: Wintershall, 34119 Kassel, Germany.
*E-mail of corresponding author: bmass@statoil.com

Acknowledgements

Funding for this work and approval for publication is gratefully acknowledged from Norske Shell, Statoil, Total and Petoro. We thank Roxar for providing academic licenses for RMS® software with which models were gridded and visualized, and Schlumberger for providing academic licenses for Petrel® and ECLIPSE 100 software. The authors would like to thank Rodmar Ravnås and Marcus Sarginson (Norske Shell) for advice and guidance in the research project, as well as M.Sc. students Ayana Bréhéret and Justine Daboer (Imperial College London). We gratefully acknowledge C. Hern, M. Sweet, F. Whitehurst and an anonymous reviewer for their constructive reviews and editorial comments.

Abstract

Tidal heterolithic sandstones are often characterized by millimeter- to centimeter-scale intercalations of mudstone and sandstone. Consequently, their effective flow properties are poorly predicted by (1) data that do not sample a representative volume, or (2) models that fail to capture the complex three-dimensional architecture of sandstone and mudstone layers. We present a modelling approach in which surfaces are used to represent all geologic heterogeneities that control the spatial distribution of reservoir rock properties ("surface-based modeling"). The workflow uses template surfaces to represent heterogeneities classified by geometry rather than length-scale. The topology of the template surfaces is described mathematically by a small number of geometric input parameters and models are constructed stochastically. The methodology has been applied to generate generic, 3D mini-models (9 m^3 volume) of cross-bedded heterolithic sandstones representing trough and tabular cross-bedding with differing proportions of sandstone and mudstone, using conditioning data from two outcrop analogs from a tide-dominated deltaic deposit. The mini-models capture the cross-stratified architectures observed in outcrop and are suitable for flow simulation, allowing computation of effective permeability values for use in larger-scale models. We show that mudstone drapes in cross-bedded heterolithic sandstones significantly reduce effective permeability and also impart permeability anisotropy in the horizontal as well as vertical flow directions. The workflow can be used with subsurface data, supplemented by outcrop analog observations, to generate effective permeability values to be derived for use in larger-scale reservoir models. The methodology could be applied to the characterization and modeling of heterogeneities in other types of sandstone reservoirs.

Introduction

Heterolithic sandstones are commonly generated by tidal processes in shallow marine environments, such as deltaic and estuarine depositional systems. In these tidally-influenced environments, the main current direction varies depending on the relative strength of tidal currents over daily to twice-daily cyclical time periods, and the interaction of tidal currents with waves and river currents (e.g. Dalrymple and Choi, 2007). Sand is transported as bedload by strong currents to form ripples and dunes during periods of rising (flood) and falling (ebb) tide, and mudstone drapes are deposited during intervening slack-water periods. Depending on the flow regime, the mudstone drapes are more or less continuous over the sandy bedforms (Reineck and Wunderlich, 1968; Reineck and Singh, 1980; Nio and Yang, 1991). This results in interstratified, millimeter- to centimeter-thick sandstone and mudstone layers that are deposited over multiple tidal cycles, and form the fine-scale heterogeneities that are characteristic of heterolithic tidal sandstone reservoirs. The distribution of mudstones and sandstones is delimited by a hierarchy of stratigraphic surfaces including (in order of increasing length scale): (1) lamina boundaries and reactivation surfaces that record incremental migration of bedforms, (2) the erosional bases of beds and bedsets, (3) boundaries between facies and facies associations, and (4) sequence stratigraphic surfaces. These four levels of stratigraphic surfaces define the multi-scale architecture and connectivity of mudstone and sandstone layers which, in turn, exerts a key control on the flow of gas, oil and water during field production (Weber, 1986; Jackson *et al.*, 2003, 2005; Ringrose *et al.*, 2005; Nordahl *et al.*, 2005, 2006; Nordahl and Ringrose, 2008).

The presence of these multi-scale heterogeneities in heterolithic tidal sandstone reservoirs ensures that the characterization of effective reservoir properties such as permeability, relative permeability, and capillary pressure, is a recurring problem (e.g. Martinius *et al.*, 2005). Effective reservoir properties are typically derived from subsurface well data such as wireline logs and well tests, combined with laboratory measurements on cores and core plugs. Laboratory-derived reservoir properties are measured at a length scale that is small (of the order centimeters for a typical core plug) compared to the dimensions of grid cells in reservoir simulation models (of the order tens to hundreds of meters in plan-view, and 10's cm to meters in the vertical direction). In the case of tidal heterolithic sandstones, lateral and vertical variations in the continuity and connectivity of sandstone and mudstone laminae (e.g. meters to tens of meters) are not sampled by either subsurface well data or laboratory measurements. However, effective reservoir properties in heterolithic units are highly dependent on the volume sampled (Norris and Lewis, 1991; Jackson *et al.*, 2003, 2005; Nordahl and Ringrose, 2008). Consequently, effective reservoir properties derived solely from subsurface and laboratory data in such heterolithic units are not representative of reservoir behavior; instead, models are required that capture the continuity and connectivity of sandstone and mudstone laminae at the appropriate length-scale.

Two different methodologies have been used to create such models, which both use stratigraphic surfaces to reproduce multi-scale heterogeneities. The first approach mimics depositional processes by generating and translating bedforms with a particular geometry according to user-defined inputs such as current velocity and sediment accumulation rate through time (e.g. Rubin, 1987; Wen *et al.*, 1998; Rubin and Carter, 2005). Cross-stratification is defined by the preserved remnants of the bedform-bounding surfaces, while lithologies are distributed according to the local current velocities during deposition. This process-based methodology has been used to generate highly realistic models of near-wellbore regions (with dimensions of the order 0.3 x 0.3 x 2 m) (Nordahl *et al.*, 2005; Ringrose *et al.*, 2005). However, process-based methodologies suffer from two problems. First, the models cannot be conditioned directly to data available from outcrop or subsurface measurements. Second, the required input parameters describing ancient depositional properties, such as variations in current velocity and sediment availability, are highly uncertain and have to be selected so as to produce a model that matches the preserved rock architecture observed in core or outcrop; this is a complex and non-unique inversion problem that is difficult to solve.

The second approach uses geometric and lithologic data from the subsurface in conjunction with outcrop analogs to directly condition reservoir models (e.g. White and Barton, 1999; Willis and White, 2000; White *et al.*, 2004; Jackson *et al.*, 2009; Sech *et al.*, 2009). Jackson *et al.* (2005) generated 3D models of rock samples (with dimensions of order 0.5 x 0.5 x 0.3 m) from heterolithic tidal sandstones observed at outcrop using serial 2D sectioning, scanning and surface reconstruction techniques. Their methodology yields models that are directly conditioned to observed geologic data, but its application relies on selection of an appropriate analog (or analogs) for the reservoir facies to be characterized. Furthermore, such a method is time-consuming, difficult to replicate, and leads to the creation of deterministic models that do not capture uncertainty in sandbody proportions, geometry and connectivity.

In this study, a surface-based modeling workflow is presented, which is then used to produce stochastic models of heterolithic, cross-bedded tidal sandstones conditioned to outcrop or subsurface data. A cross-bedding template surface is used in order to define and populate a rock volume. The 3D morphology of the template surface is defined by purely geometric input parameters that, in the case documented herein, were defined using measurements from an outcrop analog (the Eocene Dir Abu Lifa Member, Western Desert, Egypt; Bown and Kraus, 1988; Legler *et al.*, 2013). The models incorporate three of the four hierarchical levels of heterogeneity for heterolithic tidal sandstone reservoirs described above: (1) lamina boundaries and reactivation surfaces, (2) erosional bases of beds and bedsets, and (3) boundaries between facies and facies associations. The paper has four objectives. First, we present the new surface-based modeling workflow. Second, we identify the geometric input parameters required for the modeling process and extract a range of values for these parameters from statistical analysis of the outcrop analog dataset. Third, we describe two generic models that reproduce: (1) trough cross-bedding dominated by muddy toesets and with a relatively low sandstone content (89%), and (2) tabular cross-bedding dominated by sandy foresets and with a higher sandstone content (94%). Finally, we use flow-simulation to calculate the effective permeability of the models in order to demonstrate the effectiveness of the surface-based modeling workflow and its application to build models suitable for flow simulation. In a companion paper (Massart *et al.*, 2016, this issue), the surface-based methodology has been used to create a set of mini-models in order to investigate the range of effective permeability in heterolithic cross-bedded tidal sandstone facies.

Methodology

Model-construction methodology

The stratigraphic surfaces that define sedimentary structures within tidal sandstone reservoirs can be categorized by their 3D geometries, irrespective of length scale: (1) planar surfaces (parallel bedding; erosional or conformable facies contacts), (2) concave-upward surfaces (sigmoidal bedding or cross bedding structures; channelized erosional contacts), or (3) wavy surfaces (wavy-bedding, lenticular-bedding and flaser-bedding structures; irregular erosional contacts). The surface-based methodology uses these scale-independent stratigraphic surface geometries by modeling rock volumes within which surfaces share a common geometric template. This methodology comprises the following three steps (Figure 1).

(1) The volume of rock to be modeled is subdivided into "elemental volumes" delimited by a basal and a top surface. In each elemental volume, the heterogeneities are associated with stratigraphic surfaces that have the same 3D geometry. The elemental volumes have uniform shapes, but their dimensions can be varied. The model volume is filled with elemental volumes until an appropriate 3D density is reached, in an approach analogous to object-based modeling (e.g. Haldorsen and Damsleth, 1990). Rules of superposition and erosion are applied to the elemental volumes to mimic their chronostratigraphic ordering. For example, if the elemental volumes represent erosionally-based sediment bodies, then each elemental volume is eroded by the basal surfaces of "younger" elemental volumes.

(2) Each elemental volume contains only one type of stratigraphic surface, the geometry of which is defined by a "template surface". The 3D geometry of the template surface is defined mathematically. Each elemental volume is then filled with numerous stratigraphic surfaces derived from the single template surface, following rules introduced by the user to define, for example, the vertical and horizontal surface spacing. The vertical and lateral extent of the surfaces within each elemental volume is controlled by the vertical and lateral extent of the elemental volume.

(3) Once every elemental volume has been filled with template surfaces, a facies code is assigned to the geologic domains defined by the surfaces, or to the surfaces themselves. The facies codes constrain the modeling of fine-scale petrophysical properties such as porosity and permeability.

(4) The surface-based model is then gridded for flow simulation. The grid is constructed around the stratigraphic surfaces, in order to retain the geometries defined by the surfaces and minimize the number of active grid cells required for flow simulation (Jackson *et al.*, 2005, 2009, 2013, 2015; Sech *et al.*, 2009). The resulting models are geometrically accurate and computationally efficient, although the complex grid architectures may introduce numerical artefacts in conventional reservoir simulators (described in more details in Massart *et al.*, 2016; see also Graham *et al.*, 2015).

Application to heterolithic, cross-bedded tidal sandstones

The three-step methodology described above is applied herein to the modeling of heterolithic, cross-bedded tidal sandstones (Figure 1). Cross-bedded sandstones are common in a wide range of depositional environments, including those influenced by tides (e.g. Harms *et al.*, 1982; Rubin, 1987; Ashley, 1990). Cross-beds result from the migration of dunes (or megaripples *sensu* Allen, 1968, or sand waves *sensu* Allen, 1980) in response to a unidirectional current. Dunes develop straight crests (2D dunes) under low current velocities, and sinuous or discontinuous crests (3D dunes) under higher current velocities (Dalrymple *et al.*, 1978; Allen, 1980; Elliott and Gardiner, 1981; Middleton and Southard, 1984). Any dip-section (parallel to the main current direction) gives the same geometry for tabular (or planar) cross-beds resulting from the migration of 2D dunes, whereas trough cross-beds resulting from the migration of 3D dunes have a more variable dip-section geometry. Each migrating dune is preserved as a cross-bed set with an erosional base, whose geometry and extent reflect the morphology and trajectory of the scoured area in front of the migrating dune. In the case of 2D dunes, the unidirectional current is dispersed along a large area downstream of the dune crest, such that an extensive planar erosion surface of low scour capacity is formed (Harms *et al.* 1982). In the case of 3D dunes, the current is focused downstream of the migrating dune into scour pits, which migrate to produce a curved, concave-upwards erosion surface (Dalrymple *et al.*, 1978; Harms *et al.*, 1982). Cross-beds produced by dune migration are commonly stacked into larger sediment bodies of characteristic internal architecture. For example, the deposits of larger bedforms, such as bars, accumulate via the accretion of cross-beds that record the migration of smaller, superposed bedforms, such as dunes and ripples, across the bar surface. Tidal bars migrate laterally into adjacent channels due to changes in tidal flow patterns or interactions with other processes (e.g. variations in wave climate or fluvial discharge). Consequently, tidal bar deposits can be comprised entirely of stacked cross-bed sets, corresponding to the preserved remnants of repeated dune migration (Allen, 1980; Dalrymple, 1984; Ashley, 1990).

Modeling of elemental volumes

A volume of 9 m^3 (3 x 3 x 1 m) of cross-bedded sandstone is considered in this study; in a companion paper (Massart *et al.*, 2016), we demonstrate that this volume comfortably exceeds the minimum volume (the representative elementary volume or REV) required to calculate representative values of effective permeability in these dune scale cross-bedded heterolithic units. At this length scale, the elemental volumes comprise tabular and trough cross-bed sets, representing the preserved parts of 2D and 3D dunes in a tidal bar succession, respectively. In each cross-bed set, the key heterogeneities captured are mudstone drapes along foreset-toeset surfaces and each set corresponds to an elemental volume. The model volume of 9 m^3 here samples approximately 6 cross-bed sets and 600 foreset-toeset surfaces, based on outcrop-analog data presented in a later section.

Cross-bed set boundaries correspond to the preserved remnants of the erosional surface developed downcurrent of migrating 2D- or 3D-dunes (Figure 2 A). Observations of modern tidal dunes show that this erosional surface has a curved, elliptical shape in the strike direction (orthogonal to the main paleocurrent direction, Figure 2 B). As the dunes migrate, the resulting erosional surface is a downstream-amalgamated composite of the elliptical strike-sections that record the successive positions of the deepest part of the scour pool in front of the dune (Figure 2 B). In order to mimic the 3D geometry of this composite erosional surface, the corresponding elemental volumes have been modeled here as ellipsoids (Figures 3, 4). The model volume is thus subdivided into ellipsoidal elemental volumes that correspond to cross-bet sets, with tops that are truncated by the basal surfaces of overlying elemental volumes (Figure 1 B). The elemental volumes are modeled stochastically using the input parameters summarized in Table 1. For each parameter, the modeling algorithm can use a single value, or a distribution characterized by a mean value and a standard deviation.

Modeling template surfaces within elemental volumes

Each ellipsoidal elemental volume representing a cross-bed set contains multiple foreset-toeset template surfaces of uniform geometry. The spacing of foresets and toesets, and their associated mudstone drapes, is typically rhythmic, reflecting a hierarchy of periodic cycles in tidal current velocity (e.g. Nio and Yang, 1991). The shortest tidal cycle is semi-diurnal (c. 12 hour period), and is characterized by the alternation of flood and ebb current stages, separated by slack-water periods when the current velocity is zero. During slack-water periods, mud particles and clay aggregates (flocs) are deposited to form mudstone drapes over sandy bedforms (Allen, 1981; Dalrymple *et al.*, 2003). In an idealized semi-diurnal tidal cycle, both the ebb and flood tides are recorded by deposition of a sand lamina on the lee face (foreset) of a dune (Visser, 1980). Slack-water periods are recorded by mudstone drapes that separate the foreset-toeset sandstone laminae representing the ebb-tidal and flood-tidal currents. The tide is typically asymmetric, such that the ebb-tidal or flood-tidal currents are either of unequal velocity or are physically separated around the bar form (Visser, 1980). The dominant tide is represented by thicker foreset-toeset sandstone laminae and the subordinate tide by either thinner laminae or erosion (reactivation) surfaces.

An idealized, fully preserved semi-diurnal tidal cycle is thus represented by two sandstone laminae and two mudstone drapes ("paired mudstone drapes" or "mud couplet"; Visser, 1980) that constitute one tidal bundle (Boersma, 1969). Longer tidal cycles, which are commonly preserved as rhythmic variations in the thickness of sandstone laminae and mudstone drapes within cross-bed sets, are diurnal (c. 24 hour period) and spring-neap (c. 14 day period) cycles. Superposition of the different tidal cycles, combined with other sediment transport processes, leads to preservation of sandy foresets and muddy toesets. A vertical profile through dune toeset deposits typically exhibits rhythmic alternation of millimeter- to centimeter-thick, wavy-bedded mudstone and sandstone laminae (Reineck and Singh, 1967). The transition between the foreset and toeset of each lamina in a cross-bed set is marked by a gradual reduced downcurrent curvature. The resulting foreset-toeset geometry may be referred to as "shovel" shaped (Van den Berg *et al.*, 2007). In a dip-section, the shape of the foreset part is therefore approximated by a parabolic curve, and that of the toeset part is approximated by a straight line:

$$\begin{cases} \text{Foreset: if } x > 0, z(x) = Ax^2 \\ \text{Toeset: if } x < 0, z(x) = 0 \end{cases} \quad (1)$$

where x is the dip-direction coordinate, and z is the vertical coordinate, relative to the junction point O between the flat toeset part and the concave-upward foreset part (which is defined to be the origin, $x = 0$, $z = 0$). The whole toeset-foreset surface is then rotated by an angle α, which corresponds to the dip angle of the toeset. Equation (1) becomes:

$$\begin{cases} \text{Foreset: if } x > 0, z(x) = \dfrac{\cos\alpha - 2xA\cos\alpha\sin\alpha - \sqrt{\cos^2\alpha - 4Ax\sin\alpha}}{2A\sin^2\alpha} \\ \text{Toeset: if } x < 0, z(x) = x\tan\alpha \end{cases} \quad (2)$$

Notice that both equations have the same derivative $z'(x = 0) = \tan\alpha$ at the junction point O, so that the curve is continuous from the toeset part to the foreset part of the surface.

In a strike section with coordinate y, the foreset and toeset geometry reflects the erosional scour at the base of the migrating dune, so that the resulting cross-section in the strike direction corresponds to trough or tabular cross-beds. Successive foreset-toeset surfaces are parallel to each other, and parallel to the erosional base of the cross-bed set (i.e. elemental volume). Consequently, equation (2) is generalized for any *(x,y)* direction:

$$\begin{cases} \text{Foreset: if } x > 0, z(x,y) = \left[\dfrac{\cos\alpha - 2xA\cos\alpha\sin\alpha - \sqrt{\cos^2\alpha - 4Ax\sin\alpha}}{2A\sin^2\alpha}\right] + \left[\sum_1^i T_{T_i} + B(x,y)\right] \\ \text{Toeset: if } x < 0, z(x,y) = \left[x\tan\alpha\right] + \left[\sum_1^i T_{T_i} + B(x,y)\right] \end{cases} \quad (3)$$

where *B(x,y)* describes the 3D ellipsoidal shape of the basal surface of the cross-bed set (i.e. elemental volume):

$$B(x,y) = (H_E/2)\sqrt{1 - \frac{x^2}{(L_E/2)^2} - \frac{y^2}{(W_E/2)^2}} \tag{4}$$

The term $\sum_{1}^{i} T_{T\,i}$ corresponds to the cumulative toeset thickness, with T_T corresponding to the individual toeset thickness. Every cross-section of one foreset-toeset surface in the strike direction is an ellipse parallel to the erosional base of the cross-bed set. In particular, for $x = 0$, the strike cross-section curve links all junction points O of any given foreset-toeset surface, creating a junction line Oy, simplifying equations (3) and (4) to yield:

$$z(x=0,y) = \sum_{1}^{i} T_{T\,i} + (H_E/2)\sqrt{1 - \frac{y^2}{(W_E/2)^2}} \tag{5}$$

In order to populate the ellipsoidal elemental volumes with foreset-toeset template surfaces, the input parameters summarized in Table 1 are required (Figures 1 C, 5). Toeset thicknesses T_T (Figure 5) are generally too small to be routinely measured directly from cores and outcrop analogs with high accuracy (< 1 cm). Therefore we calculate T_T indirectly from two other parameters: the dip angle of the toesets α and the angle of dune climb δ (Figure 5). The dip angle α corresponds to the angle of rotation applied to the parabolic curve representing the foreset-toeset template surface. T_T is then given by:

$$T_T = F_T \sin(\alpha + \delta) \tag{6}$$

Modeling of mudstone drapes along foreset-toeset surfaces

If the succeeding flood-tide or ebb-tide is sufficiently strong, then mudstone drapes can be partially or entirely eroded, such that only one mudstone drape and one reactivation surface may be preserved during one flood-and-ebb tidal cycle (de Mowbray and Visser, 1984). Thus, the foreset-toeset surfaces modeled in the previous step may not be entirely covered by mudstone. The extent and continuity of mudstone drapes is defined using a function to describe the mudstone frequency in the dip direction along the stratigraphic surfaces, relative to a well-defined position on the surfaces. Mudstone drapes are modeled as elliptical patches of mudstone that are placed stochastically on each surface. Where they overlap, new patches erode older patches, so the patches coalesce to produce drapes with complex geometries. The length and aspect ratio of each elliptical patch is also modeled stochastically. Patches are placed on the stratigraphic surfaces until a user-specified proportion of their area is reached, following the methodology of Jackson and Muggeridge (2000). The mudstone frequency function denotes the probability that a patch will be placed at a certain location along each surface. The foreset part of each surface is modelled first; the mudstone drape coverage is then calculated at the transition between foreset and toeset parts (line *Δ* in Figure 5), and this calculated value is then used as the target mudstone drape coverage for the toeset parts, in order to ensure mudstone drape coverage continuity between the foreset and toeset parts. Consequently, toeset and foreset parts of each surface can have different mudstone drape coverage, allowing us to capture the muddy toesets typically observed in outcrop. The distribution of mudstone drapes along each surface is controlled by the chosen mudstone frequency function *f*, which is determined here from outcrop analog data. The following equation has been used to define *f*:

$$f\left(\frac{x-x_O}{x_F-x_O}\right)=\frac{M}{1+e^{\left(N\left(\frac{x-x_O}{x_F-x_O}\right)+O\right)}} \qquad (7)$$

where x_O corresponds to the coordinate of the junction point *O* between foreset and toeset sections, x_F corresponds to the coordinate of the point *F* marking the preserved top of the foreset, and *M*, *N* and *O* are constants that are chosen to fit data extracted from the outcrop analog. Such data could also be extracted from process-based models.

Mudstone drape thickness is user defined in the models and, at present, is assumed to be constant for each drape. As mudstones are modeled as barriers to flow, their thickness has no impact on their flow properties; however, drape thickness does affect the total volume of the model that is occupied by mudstone. Here we have assumed a mud drape thickness of 3.5 mm, which is a typical mean value encountered in heterolithic cross-bedded tidal sandstones (Terwindt, 1971; Nio and Yang, 1991; Martinius and Van den Berg, 2011). Measurements of mudstone drape thickness could be taken from core datasets for application to a specific reservoir, or from a suitable outcrop analog. The input parameters required for modeling mudstone drapes are summarized in Table 1 (Figure 1 D).

Outcrop analog data analysis to define model input parameters

The input parameters required to construct the models of heterolithic, cross-bedded tidal sandstones were collected from an exceptionally well-exposed outcrop analog (see below), which enabled the 3D geometry of the elemental volumes, template surfaces and mudstone distribution to be evaluated quantitatively.

The studied outcrop analog forms part of the Eocene Dir Abu Lifa Member, located in the Western Desert of Egypt (Figure 6). The Dir Abu Lifa Member was deposited in a shallow-marine environment protected from wave energy, resulting in a predominance of tidal processes (Abdel-Fattah *et al.*, 2010; Legler *et al.*, 2013). The lower part of the Dir Abu Lifa

Member consists largely of tidal bar and channel deposits that are stacked laterally and vertically (Legler *et al.*, 2013). The lower parts of tidal bar deposits typically comprise heterolithic, cross-bedded sandstones.

The lower Dir Abu Lifa Member is exposed in a continuous escarpment over 20 km long, which is cut by multiple canyons that provide some three dimensional control (e.g. Legler *et al.*, 2013). The datasets used in this study are taken from two locations, labelled Gecko Nose and Butterfly Canyon in Figure 6. Gecko Nose is a small promontory which is defined by two cliff faces that trend approximately WNW-ESE and SSW-NNE, nearly perpendicular to each other (Figures 6, 7). The promontory exposes stacked trough and tabular cross-bedded sandstones, interpreted as the deposits of tidal bars in a channel belt (the “yellow channel” in the Gebel Sagha area of Legler *et al.*, 2013). The WNW-ESE-oriented cliff face (N110-N290) is 17 m long, and the SSW-NNE-oriented cliff face (N030-N210) is 12 m long. Paleocurrent measurements from the cross-beds are oriented towards N230, indicating that the WNW-ESE- and SSW-NNE-oriented cliff faces provide close to strike and dip sections, respectively. The slight deviation from the mean dip direction indicated by the paleocurrent data does not significantly impact the geometry of the modeled cross-bed sets.

Butterfly Canyon contains a larger promontory than Gecko Nose, defined by two cliff faces that trend approximately N-S and W-E. The Butterfly Canyon outcrop also exposes stacked trough and tabular cross-bedded sandstones deposited in bars occupying an isolated channel in a tidal flat environment (the Wadi Ghorab area of Legler *et al.*, 2013). Paleocurrent measurements from the cross-beds are oriented towards N196, indicating that the W-E- and N-S-oriented cliff faces again provide close to strike and dip sections, respectively. Tidal bar deposits exposed at Butterfly Canyon are sandier than those at Gecko

Nose, and the two deposits are considered to be end-members of the same heterolithic, cross-bedded tidal sandstone facies.

High-resolution photographs and precise sketches were collected from the cliff faces of both localities, in order to capture the dimensions and geometries of cross-bed sets. Photographs were collected using no-distortion lenses. Each cross-bed set in the Gecko Nose outcrop has been reconstructed from the high-resolution photographs and scaled using the sketches. The boundaries of the cross-bed sets and their constituent foreset-toeset surfaces have been traced on the reconstructed pictures, enabling quantitative, statistically representative datasets to be compiled for the various input parameters of the modeling methodology described above. All values are summarized in Table 1.

To define the dimensions of ellipsoidal elemental volumes (L_E , W_E and H_E) we used data from the Gecko Nose outcrop. W_E and H_E were determined from 12 trough cross-bed set boundaries (identified in Figure 8 A) from the strike-oriented face, using the method presented in Figure 4. The dataset was limited to cross-bed sets with sufficient exposure to allow a best fit elliptical curve, with dimensions corresponding to W_E and H_E , to be fitted to their erosional basal surfaces (Figure 4 C). L_E was estimated from cross-bed sets exposed on the dip-oriented face. ,The basal boundaries of all trough cross-bed sets in the dip-oriented face were continuous and nearly planar over the 12 m extent of the face, suggesting $L_E >> W_E$. No pinch-outs were observed. The elemental volume density *D*, was determined from the total of 90 trough cross-bed sets observed at the Gecko Nose location within a volume of 12 x 17 x 3 m, such that *D* is equal to 0.15 elemental volumes per m^3. The dimensions of the preserved parts of the ellipsoidal elemental volumes (L_A , W_A and H_A) were determined using data from both outcrops. W_A and H_A were determined from the strike-oriented face of Gecko Nose (Figure 8 B). Values of both W_A and H_A define log-normal distributions (Figure 9). All of the cross-bed sets observed in the dip-oriented face of Gecko Nose are laterally continuous, in which case $L_A > 12$ m. At Butterfly Canyon, L_A is observed in one cross-bed set to equal 25 m, which is the value used thereafter.

In order to determine the degree of curvature *A*, the 90 foreset-toeset surfaces contained in three well-preserved trough cross-bed sets in the Gecko Nose outcrop (numbered 34, 50 and 52 in Figure 8 A) have been extracted from photomontages. The three cross-bed sets show clear, dip-oriented cross-sections of the foreset-toeset surfaces. The foreset-toeset surfaces are rotated in our analysis so that their toesets are horizontal. For each foreset-toeset surface, the junction point *O* is identified. All the foreset curves are then translated to the same origin and a best-fit parabolic curve is fitted to the data (Figure 10). To determine the foreset thickness F_T, the sandstone laminae thicknesses comprised between the 544 foreset-toeset surfaces contained in 12 studied cross-bed sets (identified in Figure 8 A) have been measured after extraction of the surfaces from photomontages. A log-normal distribution of F_T values is observed (Figure 11). The dip angle of the toesets α has been measured on photopanoramas of the NNE-SSW-oriented (oblique dip-oriented) face of Gecko Nose. The angle of dune climb δ has been determined by generating a best-fit line through the foreset-to-toeset junction points *O* of laminae in each of the studied cross-bed sets.

To define the mudstone frequency function *f*, the positions of mudstone drapes along the same 90 foreset-toeset surfaces of the three cross-bed sets used to determine the parameter *A* (numbered 34, 50 and 52 in Figure 8 A) have been extracted from photomontages. From this dataset, a frequency distribution of mudstone drape presence relative to position along the foreset has been determined using equation (7) to define a best-fit curve (Figure 12).

Results

Models constructed from outcrop analog data

The 3D models of heterolithic, cross-bedded tidal sandstones are based on those observed at the Gecko Nose and the Butterfly Canyon localities. Generic models have been generated using input parameters derived from both localities (Figures 13 and 14; Table 1). The models are stochastically generated using the data reported in the previous section, except for the elemental volumes, whose coordinates inside the model are extracted directly from photomontages of the two outcrop localities so that the traces of the elemental volumes in cross-sections of the model accurately reproduced the cross-bed set boundaries of the outcrop sections. Both models are 9 m^3 in volume (3 x 3 x 1 m), and contain four partially preserved ellipsoidal elemental volumes in the case of the Butterfly Canyon model and six partially preserved ellipsoidal elemental volumes in the case of the Gecko Nose model. The model volumes are approximately five orders of magnitude larger than the volume of a typical core plug (c. 20 cm^3). Around 500 foreset-toeset surfaces are populated in in the Gecko Nose model, whereas only 170 of the same surfaces are present in the Butterfly Canyon model (parameter N_{CB} in Table 1). Note that the two outcrop localities both display examples of tabular and trough cross bedding. However, the Gecko Nose model shown here contains only trough cross-beds, and the Butterfly Canyon model contains only tabular cross-beds, reflecting the specific parts of the outcrops modelled. The mudstone drape coverage that was chosen for both models is equal to 25% along the foreset parts and 57% along the toeset parts of the foreset-toeset surfaces; the foreset drape coverage was extracted from outcrop data, while the toeset drape coverage is given by the fraction at the foreset-toeset junction resulting from the chosen mudstone frequency function (Figure 12), as outlined in the methodology.

A comparison between the outcrop cliff faces of Gecko Nose and Butterfly Canyon, and the corresponding generic models is presented in Figure 15. The models honor the geometry of the cross-bed set boundaries, in both strike and dip directions, which validates the choice of having cross-bed sets represented as ellipsoidal elemental volumes (Figures 2, 3 and 4). The input average foreset thickness F_T is respected as observed at the outcrop locations, with F_T being smaller for the Gecko Nose model than for the Butterfly Canyon model. The Gecko Nose model is relatively mudstone-rich (sandstone volume fraction $V_S / V_T = 0.89$), as it comprises trough cross-beds containing a relatively high proportion of toesets and thin foresets (foreset thickness F_T = 5.85 cm and foreset to toeset volume ratio $R_{F/T}$ = 6.5 : 1, Table 1) due to the high dune climb angle of δ = 5°. The Butterfly Canyon model is comparatively mudstone-poor (sandstone volume fraction $V_S / V_T = 0.94$), as it comprises tabular cross-beds dominated by thicker foresets (foreset thickness F_T = 10.0 cm and foreset to toeset volume ratio $R_{F/T}$ = 24 : 1, Table 1), with a low dune climb angle δ = 0°.

The distribution of mudstone drapes along the cross-bedding surfaces closely matches the distribution observed at outcrop. Both in the models and at outcrop, some mudstone drapes appear continuous along the entire cross-bedding surface, from the toeset part to the top of the foreset at the top boundary of the cross-bed set. In most cases, the mudstone drapes in the models are discontinuous over the entire length of the cross-bedding surfaces in dip-oriented cross-sections, but the discontinuities are limited in the strike direction, which is again a close match to outcrop observations. Discontinuities of the mudstone drapes in the models are mostly located at the top of the foreset part of the cross-bedding surfaces, following the trend of the input mudstone drape frequency function defined from statistical analysis of outcrop data (Figure 12).

Calculation of effective permeability

The method to calculate effective permeability is presented in the companion paper (Massart *et al.*, 2016) and we report only the results here for the two models shown in Figures 13 and 14. We report the effective permeability as a normalized value, expressed as a fraction of the sandstone permeability:

$$k_e^n = \frac{k_e}{k_{sand}} \tag{8}$$

The results reported in this way are independent of the value of sandstone permeability used in the models; moreover, the normalized effective permeability can be rescaled to any value of sandstone permeability obtained from core or mini-permeameter measurements.

The effective permeability of the model volume has been extracted in three orthogonal directions: the horizontal effective permeability down depositional dip k_d , the horizontal effective permeability along depositional strike k_s , and the vertical effective permeability k_v . The mean value for horizontal permeability k_h is defined as the arithmetic average between k_s and k_d such as $k_h = (k_d + k_s)/2$ (Jackson *et al.*, 2003). The results for each model are summarized in Table 2. Despite the relatively low fraction of mudstone in the models, the presence of the mudstone drapes significantly reduces both horizontal and vertical permeabilities, and introduces permeability anisotropy in the horizontal as well as the vertical directions : $k_s \neq k_d$ and $k_v << k_h$. For the trough-cross bedded model of Gecko Nose, the dip-oriented horizontal permeability (k_d^n = 47.5%) is only 65% of the strike-oriented horizontal permeability (k_s^n = 72.8%), as the flow must cross a larger number of mudstone-draped foresets when flowing down depositional dip as opposed to along depositional strike. The k_v/k_h ratio is reduced to only 0.040, reflecting that vertical flow must also cross numerous mudstone-draped foresets. The horizontal permeability anisotropy of the tabular cross-bedded Butterfly Canyon model is less pronounced than in the trough-cross-bedded Gecko Nose model, reflecting the lower mudstone fraction and greater strike-oriented continuity of foreset-toeset sandstone laminae in the former model: the dip-oriented horizontal permeability (k_d^n = 70.0%) is 78% of the strike-oriented horizontal permeability (k_s^n = 90.0%). Despite the lower overall mudstone fraction, the k_v/k_h of the tabular cross-bedded Butterfly Canyon model is one order of magnitude smaller (at 0.003) than the value of the trough cross-bedded model. Mudstone drapes are approximately three times more numerous in the trough cross-bedded model ($N_{CB} \approx 500$) than in the tabular cross-bedded model ($N_{CB} \approx 170$); they are more densely spaced and laterally continuous in the toesets of the trough cross-bedded model because of the high values of the toeset dip angle α. Moreover, the sandstone volume fraction in the toesets of the tabular cross-bedded model is 0.26, which is less than half of the sandstone volume fraction in the toesets of the trough cross-bedded model, despite the common value of mudstone drape coverage of 57% in both models. The smaller value of k_v/k_h ratio in the tabular cross-bedded model arises from the closer spacing of mudstone-draped toesets, higher density of toeset surfaces, and consequent lower sandstone volume fraction in the toeset parts of cross-bed sets.

For the two models studied, the normalized effective permeability values can be rescaled to any measured sandstone permeability to yield estimates of effective permeability suitable for use in larger-scale reservoir models (Figure 16). For example, if the measured permeability of the sandstone was 500 md, then the trough-cross bedded (Gecko Nose) model yields permeability values of k_d = 238 md, k_s = 364 md and k_v = 12 md, while the tabular cross-bedded (Butterfly Canyon) model yields permeability values of k_d = 350 md, k_s = 450 md and k_v = 10 md. If the permeability of the sandstone was lower at 100 md, effective permeabilities are proportionately reduced as well, yielding k_d = 48 md, k_s = 73 md and k_v = 3 md for the trough cross-bedded model, and k_d = 70 md, k_s = 90 md and k_v = 2 md for the tabular cross-bedded model. Effective permeability values from a broader range of model geometries and mudstone fractions are reported in the companion paper (Massart *et al.*, 2016).

The modeling workflow reported here can be applied to create appropriate models for the calculation of effective permeability values depending on the geometric characteristics of the heterogeneity surfaces of any tidal cross-bedded heterolithic sandstone observed at outcrop location or in subsurface. The required input parameters and methods for measuring each of them are summarized in Figure 1. The main orientation of cross-bed sets (i.e. the paleocurrent) and its standard deviation can be deduced from dipmeter logs. The style of cross-bedding is easily recognizable from the trace of the cross-bedding plane around the core or from borehole image logs. The tracing of the cross-bedding plane on well imagery can be considered for more precision, as core observations are typically only possible on one half of the core. The foreset thickness F_T can be measured on core from a representative number of occurrences, even if the typical width of a core (8 – 20 cm) prevents observation of a complete spring-neap cycle that displays cyclical variation of foreset thickness. The foreset to toeset ratio $R_{F/T}$ can be appraised in a similar way from core observations, but with similar limitations on the degree to which core data can represent variation in the parameter. For both parameters, an outcrop analog(s) can provide a more complete dataset. As dune climb angle δ has typically small values, the ratio $R_{F/T}$ remains relatively uniform in the cross-bed set (Figures 3, 5). However, no lateral variation in $R_{F/T}$ can be deduced from core observations. Finally, the toeset dip angle α can be observed in core if toeset areas are sampled. All input parameters can be otherwise derived from statistical analysis of appropriate outcrop analogs, in a similar way to the analysis presented herein using the Dir Abu Lifa Member as an outcrop analog, with the important proviso that the degree of analogy between subsurface and outcrop cases must be established with due care.

Conclusions

This study presents a novel reservoir modeling methodology that accurately and efficiently reproduces the geometry and connectivity of sandstone and mudstone layers in heterolithic, cross-bedded tidal sandstones by stochastically modeling stratigraphic surfaces and associated heterogeneity. The model input parameters are geometric and can be derived from subsurface cores and/or outcrop analog observations. The application of the modeling methodology is demonstrated via the construction of models that represent heterogeneity in significantly larger volumes (9 m^3) than those sampled by core plugs (c. 20 cm^3), using input parameters derived from analysis of an outcrop analog. Quantitative outcrop-analog data are collated and used to constrain the geometry and spatial distribution of the small-scale heterogeneity surfaces (i.e. cross-bed set boundaries, cross-bedding foreset-toeset surfaces, and mudstone drapes). The resulting models are a close visual match to the outcrop data, such that the complex mudstone and sandstone connectivity of the heterolithic tidal deposits is accurately reproduced. The surface-based methodology is not dependent on length scale, but on the geometric configuration and hierarchical arrangement of geologic surfaces. The methodology can, therefore, be applied to a much wider range of reservoir types in which the heterogeneity style can be characterized by the 3D shape and distribution of geologic surfaces.

References cited

Abdel-Fattah, Z. A., M. K. Gingras, M. W. Caldwell, S. G. Pemberton, 2010, Sedimentary environments and depositional characteristics of the Middle to Upper Eocene whale-bearing succession in the Fayum Depression, Egypt: Sedimentology, v. 7, n°2, p. 446-476.

Allen, J. R. L., 1968, Current ripples, (Amsterdam) North-Holland.

Allen, J. R. L., 1980, Sand waves: a model of origin and internal structure: Sedimentary Geology, v. 26, p. 281-328.

Allen, J. R. L., 1981, Palaeotidal speeds and ranges estimated from cross-bedding sets with mud drapes: Nature, v. 293, p. 394-396.

Ashley, G. M., 1990, Classification of large-scale subaqueous bedforms; a new look at an old problem Journal of Sedimentary Petrology, v. 60, p. 160-172.

Boersma, J. R., 1969, Internal structure of some tidal mega-ripples on a shoal in the Westerschelde estuary, the Netherlands: Geologie en Mijnbouw, v. 48, p. 409-414.

Bown, T. M., and M. J. Kraus, 1988, Geology and paleoenvironment of the Oligocene Jebel Qatrani Formation and adjacent rocks, Fayum depression, Egypt: U. S. Geological Survey Professional paper 1452, p. 1–60.

Dalrymple, R. W., R. J. Knight, and J. J. Lambiase, 1978, Bedforms and their hydraulic stability relationships in a tidal environment, Bay of Fundy, Canada: Nature, v. 275, p. 100-104.

Dalrymple, R. W., 1984, Morphology and internal structure of sand waves in the Bay of Fundy: Sedimentology, v. 31, p. 365-382.

Dalrymple, R. W., E. K. Baker, P. T. Harris, and M. G. Hughes, 2003, Sedimentology and stratigraphy of a tide-dominated, foreland-basin delta (Fly River, Papua New Guinea), *in* Tropical Deltas of Southeast Asia; Sedimentology, Stratigraphy, and Petroleum Geology, F. H. Sidi, D. Nummedal, P. Imbert, H. Darman, and H. W. Posamentier (eds), SEPM Special Publication, v. 76, p. 147-173.

Dalrymple, R. W., and K. Choi, 2007, Morphologic and Facies Trends Through the Fluvial Marine Transition in Tide Dominated Depositional Systems: a Schematic Framework for Environmental and Sequence Stratigraphic Interpretation: Earth Science Reviews, v. 81, issues 3-4, p. 135-174.

de Mowbray, T., and M. J. Visser, 1984, Reactivation surfaces in subtidal channel deposits, Oosterschelde, Southwest Netherlands: Journal of Sedimentary Petrology, v. 54, p. 811-824.

Elliott, T., and A. R. Gardiner, 1981, Ripple megaripple and sandwave bedforms in the macrotidal Loughor Estuary, South Wales, U. K.: Special Publication International Association of Sedimentologists, v. 5, p. 51-64.

Graham, G. H., Jackson, M. D., and Hampson, G. J., 2015: “Three dimensional modeling of clinoforms within shallow-marine reservoirs: Part 1. Concepts and application: AAPG Bulletin, v. 99, p. 1013-1047.

Haldorsen, H. H., and E. Damsleth, 1990, Stochastic modeling: Journal of Petroleum Technology, v. 42, p. 404-412.

Harms, J. C., J. B. Southard and R. G. Walker, 1982, Structures and sequences in clastic rocks: SEPM short course, v. 9, Society of Sedimentary Geology.

Jackson, M. D., and A. H. Muggeridge, 2000, The effect of discontinuous shales on reservoir performance during immiscible flow: Society of Petroleum Engineers Journal, v. 5, p. 446–454.

Jackson, M. D., A. H. Muggeridge, S. Yoshida, and H. D. Johnson, 2003, Upscaling permeability measurements within complex heterolithic tidal sandstones: Mathematical Geology, v. 35, p. 499-520.

Jackson, M. D., S. Yoshida, A. H. Muggeridge, and H. D. Johnson, 2005, Three-Dimensional Reservoir Characterisation and Flow Simulation of Heterolithic Tidal Sandstones: AAPG Bulletin, v. 89, n°4, p. 507-528.

Jackson, M. D., G. J. Hampson and R. P. Sech, 2009. Three-dimensional modeling of a shoreface-shelf parasequence reservoir analog: part 2. Geologic controls on fluid flow and hydrocarbon recovery: AAPG Bulletin, v. 93, p. 1183–1208.

Jackson, M. D., J. L. M. A. Gomes, P. Mostaghimi, J. R. Percival, B. S. Tollit, D. Pavlidis, C. C. Pain, A. H. El-Sheikh, A. H. Muggeridge, and M. J. Blunt, in press, Reservoir modeling for flow simulation using surfaces, adaptive unstructured meshes and an overlapping control-volume-finite-element method: Society of Petroleum Engineers Reservoir Evaluation and Engineering.

Legler, B., H. D. Johnson, G. J. Hampson, B. Y. G. Massart, C. A.-L. Jackson, M. D. Jackson, A. El-Barkooky, and R. Ravnås, 2013, Facies model of a fine-grained, tide-dominated delta: Lower Dir Abu Lifa Member (Eocene), Western Desert, Egypt: Sedimentology, v. 60, p. 1313-1356.

Martinius, A. W., P. S. Ringrose, C. Brostrøm, C. Elfenbein, A. Næss, and J. E. Ringås, 2005, Reservoir Challenges of Heterolithic Tidal Sandstone Reservoirs in Halten Terrace, mid-Norway: Petroleum Geoscience, EAGE/Geological Society of London, v. 11, n°1, p. 3-16.

Martinius, A. W., and J. H. van den Berg, 2011, Atlas of sedimentary structures in estuarine and tidally-influenced river deposits of the Rhine-Meuse-Scheldt system: EAGE Publications BV, Houten, 298 p.

Massart, B. Y. G., M. D. Jackson, G. J. Hampson, and H. D. Johnson, 2016, Effective flow properties of heterolithic, cross-bedded tidal sandstones: Part 2. Flow simulation, AAPG Bulletin, this issue.

Middleton, G. V., and J. B. Southard, 1984, Mechanics of sediment movement: SEPM Short course 3, Society of Sedimentary Geology (Tulsa), USA.

Nio, S.-D., and C.-S. Yang, 1991, Diagnostic Attributes of Clastic Tidal Deposits: a Review *in* Clastic Tidal Sedimentology, Canadian Society of Petroleum Geologists, Memoir 16, p. 3-28.

Nordhal, K., P. S. Ringrose, and R. Wen, 2005, Petrophysical Characterisation of a Heterolithic Tidal Reservoir Interval Using a Process Based Modelling Tool: Petroleum Geoscience, EAGE/Geological Society of London, v. 11, p. 17-28.

Nordahl, K., A. W. Martinius, and A. Kritski, 2006, Time-series analysis of a heterolithic, ripple-laminated deposit (Early Jurassic, Tilje Formation) and implications for reservoir modelling: Marine Geology, v. 235, n°1-4, p. 255-271.

Nordahl, K., and P. S. Ringrose, 2008, Identifying the Representative Elementary Volume for Permeability in Heterolithic Deposits Using Numerical Rock Models: Math Geoscience, v. 40, p. 753-771.

Norris, R. J., and J. J. M. Lewis, 1991, The Geological Modeling of Effective Permeability in Complex Heterolithic Facies: Society of Petroleum Engineers paper 22692, presented at the 66th annual technical conference and exhibition, Dallas, TX, USA, 6-9 October 1991.

Reineck, H. E., and I. B. Singh, 1967, Primary sedimentary structures in the recent sediments of the Jade, North Sea: Marine Geology, v. 5, p. 227-235.

Reineck, H. E., and F. Wunderlich, 1968, Classification and origin of flaser and lenticular bedding: Sedimentology, v.11, n°1-2, p. 99-104.

Reineck, H. E., and I. B. Singh, 1980, Depositional sedimentary environments with reference to terrigenous clastics, 2nd edition, Springer-Verlag (Berlin).

Ringrose, P. S., K. Nordhal, and R. Wen, 2005, Vertical Permeability Estimation of Heterolithic Tidal Deltaic Sandstones: Petroleum Geoscience, EAGE/Geological Society of London, v. 11, n°1, p. 29-36.

Rubin, D. M., 1987, Cross-bedding, bedforms, and palaeocurrents: Concepts in Sedimentology and Paleontology, Society of Economic Palaeontologists and Mineralogists Special Publication, v. 1.

Rubin, D. M., C. L. Carter, 2005, Bedforms 4.0; MATLAB code for simulating bedforms and cross-bedding: Open-File report, U. S. Geological Survey.

Sech, R. P., M. D. Jackson, and G. J. Hampson, 2009, Three-Dimensional Modelling of a Shoreface-Shelf Parasequence Reservoir Analogue: Part 1. Surface-based Modelling to Capture High Resolution Facies Architecture: AAPG Bulletin, v. 93, n°9, p. 1155-1181.

Terwindt, J. H. J., 1971, Lithofacies of inshore estuarine and tidal inlet deposits: Geologie en Mijnbouw, v. 50, p. 515-526.

van den Berg, J. H., J. R. Boersma, and A. van Gelder, 2007, Diagnostic sedimentary structures of the fluvial-tidal transition zone; Evidence from deposits of the Rhine and Meuse: Geology en Minjbouw, v. 86, p. 287-306.

Visser, M. J., 1980, Neap-spring cycles reflected in Holocene subtidal large-scale bedform deposits: a preliminary note: Geology, v. 8, p. 543-546.

Weber, K. J., 1986, How heterogeneity affects oil recovery *in* L. W. Lake, and H. B. Carroll Jr. (eds), Reservoir characterization, Academic Press, New York, p. 487-544.

Wen, R.-J., A. W. Martinius, A. Næss, and P. S. Ringrose, 1998, Three dimensional simulation of small-scale heterogeneity in tidal deposits – A process-based stochastic method *in* A. Buccianti, G. Nardi, and A. Potenza (eds), Proceedings of the 4th Annual Conference of the International Association of Mathematical Geology, Ischia, De Frede, Naples, p. 129–134.

White, C. D., and M. D. Barton, 1999, Translating outcrop data to flow models, with applications to the Ferron Sandstone: Society of Petroleum Engineers Reservoir Evaluation and Engineering, v. 2, p. 341–350.

White, C. D., B. J. Willis, S. P. Dutton, J. P. Bhattacharya, and K. Narayanan, 2004, Sedimentology, statistics, and flow behavior for a tide-influenced deltaic sandstone, Frontier Formation, Wyoming, United States, in G. M. Grammer, P. M. Harris, and G. P. Eberli, eds., Integration of outcrop and modern analogs in reservoir modeling: AAPG Memoir 80, p. 129–152.

Willis, B. J., and C. D. White, 2000, Quantitative outcrop data for flow simulation: Journal of Sedimentary Research, v. 70, p. 788–802.

AUTHOR VITAE

Benoît Y. G. Massart works in the mature-area developments and increased oil recovery team at the Statoil research center in Bergen, Norway. He holds a Ph.D. in petroleum engineering from Imperial College London and a M.Sc. in petroleum geology from the École Nationale de Géologie de Nancy (ENSG), France. His research interests are in reservoir modeling and quantifying the influence of geologic heterogeneity on effective rock properties and fluid flow behavior, facies modeling from geophysical data, and facies and petrophysical property update in history matching in ensemble methods.

Matthew D. Jackson is the Total Professor of Geological Fluid Mechanics in the Department of Earth Science and Engineering, Imperial College, London. He holds a B.S. degree in physics from Imperial College and a Ph.D. in geological fluid mechanics from the University of Liverpool. His research interests include simulation of multiphase flow through porous media, representation of geologic heterogeneity in simulation models, and downhole monitoring and control in instrumented wells.

Gary J. Hampson is a Reader in sedimentary geology in the Department of Earth Science and Engineering, Imperial College, London. He holds a B.A. degree in natural sciences from the University of Cambridge and a Ph.D. in sedimentology and sequence stratigraphy from the University of Liverpool. His research interests lie in the understanding of depositional systems and their preserved stratigraphy, and in applying this knowledge to reservoir characterization.

Howard D. Johnson holds the Shell Chair of Petroleum Geology in the Department of Earth Science and Engineering, Imperial College, London. His main interests are in clastic sedimentology, sequence stratigraphy, reservoir characterization, and basin studies. Previously, he spent 15 years with Shell working in research, exploration and development geology, and petroleum engineering. He holds a B.Sc. degree in geology from the University of Liverpool and a D.Phil. in sedimentology from the University of Oxford.

Berit Legler is a clastic sedimentologist with Wintershall, Germany. She graduated in geology with a diplom degree and Ph.D. from the Technical University Mining Academy Freiberg, Germany. She worked as sedimentologist with RWE Dea (2005 – 2008), post-doctoral researcher at Imperial College London (2009 – 2011) and lecturer at the University of Manchester (2011 – 2013). She currently works as sedimentologist in Wintershall's Reservoir Geology technical services team.

Christopher A.-L. Jackson is currently the Statoil Professor of Basin Analysis in the Department of Earth Science and Engineering, Imperial College, UK. He obtained a B.Sc. and Ph.D. from the University of Manchester. His research interests are in the tectonostratigraphic evolution of rifts and the application of 3D seismic data to understanding the formation and filling of sedimentary basins.

Figure captions

Figure 1: Three-step methodology for constructing models of heterolithic, cross-bedded tidal sandstones. A) Subdivision of the model volume into elemental volumes, in which heterogeneities have the same length scale and geometry. In the cross-bedded sandstones modeled here, the elemental volumes are cross-bed sets represented by ellipsoids with erosional bases. Ellipsoid boundaries are represented by bold black lines. B) Each ellipsoid (i.e. cross-bed set) is populated with template surfaces that represent foreset-toeset lamina boundaries. Foreset-toeset template surfaces are represented by thin black lines. C) Each foreset-toeset template surface is then lined by mudstone drapes of variable continuity, using a mudstone frequency function, to produce D) the final model. Mudstone drapes are represented by bold gray lines. For each step, the required input parameters are listed on the right of the figure. Some parameters can be extracted from subsurface core data (*) or dipmeter logs (†), whereas others must be taken from sedimentologic analogs.

Figure 2: A) Modern 3D dune in an inter-tidal flat environment, the Wash Estuary, United Kingdom. B) Interpretation of the erosion surface resulting from migration of a dune and associated scour pool as the lower part of an ellipsoid of dimensions L_E (length, in blue), W_E (width, in red), and H_E (height, in green) relative to the horizontal reference plane Γ. Dotted lines correspond to parts of the ellipsoid beneath the dune in its present position. The yellow crescent corresponds to the dune foreset, and the gray truncated ellipse to the rippled dune toeset. The bold black line corresponds to the dip cross-section of one foreset-toeset surface.

Figure 3: A) Ancient trough cross-bed set viewed in cross-section oriented approximately along depositional dip (parallel to the paleocurrent direction), Dir Abu Lifa Member, Gecko Nose location (NNE-SSW-oriented cliff face shown with dotted line in Figures 6, 7), Western Desert, Egypt. The cross-bed set contains tidal bundles separated by double mudstone drapes in the sandy foresets, and wavy-bedded muddy toesets. B) Interpretation of the cross-bed set as the lower part of an ellipsoidal elemental volume. The purple line shows the erosional base of the cross-bed set, and the green line shows the top surface of the preserved cross-bed set (i.e. the erosional base of an overlying cross-bed set). The thin dotted line is the boundary between foresets and toesets within the cross-bed set marking the angle of climb of the dune δ. The bold black line corresponds to an interpreted foreset-toeset template surface in dip cross-section. C) The corresponding best fit ellipsoidal elemental volume is traced in 3D (see Figure 2 for colors).

Figure 4: A) Ancient trough cross-bed set viewed in cross-section oriented approximately along depositional strike (perpendicular to the paleocurrent direction which corresponds to dip direction , here out of the page), Dir Abu Lifa Member, Gecko Nose location (WNW-ESE-oriented cliff face shown with bold line in Figures 6, 7; see also Figure 8 A), Western Desert, Egypt. B) Interpretation of the cross-bed set as the lower part of an ellipsoidal elemental volume. The purple line shows the erosional base of the cross-bed set, and the green line shows the top surface of the preserved cross-bed set. The dotted arrows indicate the preserved width W_A and height H_A of the cross-bed set. The bold black line corresponds to an interpreted foreset-toeset template surface in strike cross-section. C) The erosional base of the cross-bed set has been extracted from the photomontage and a best fit elliptical curve

(in red) has been defined in order to obtain the width W_E and the height H_E of the elemental volume.

Figure 5: Detail of transition between foreset and toeset along template surfaces within an elemental volume. Input parameters required to describe the geometry of the foreset-toeset surfaces include foreset thickness F_T, toeset thickness T_T, the angle of climb of the dune δ, and the dip angle of the toeset α. The dotted line Δ corresponds to the limit between sandy foresets (light gray) and muddy toesets (dark gray), and links the junction points O of each foreset-toeset surface. The reference line Γ corresponds to the median plane of the ellipsoidal elemental volume that contains the foreset-toeset surfaces (blue ellipse in Figure 2). Once F_T is set, T_T is calculated using angles α and δ (Equation (6)).

Figure 6: A. Map of Egypt highlighting the position of the Eocene Dir Abu Lifa outcrop belt (black rectangle, south west of Cairo) B. Map of the main outcrop belt of the Dir Abu Lifa Member, highlighting the Gecko Nose and Butterfly Canyon localities. C. Close-up of the Gecko Nose outcrop, with the two studied cliff faces shown with bold lines, the continuous line corresponding to the WNW-ESE oriented section, and the dotted line to the NNE-SSW oriented cross-section (Figure 7).

Figure 7: Photograph of the two nearly perpendicular cliff faces at Gecko Nose (Figure 6). Paleocurrents in heterolithic, trough and tabular cross-bedded sandstones are oriented towards N196 (inset rose diagram), such that the WNW-ESE-oriented (bold line) and NNE-SSW-oriented cliff faces (dotted line) approximate strike and dip sections, respectively. A person is present in front of the outcrop for scale.

Figure 8: A) Photomontage of the WNW-ESE-oriented face of Gecko Nose (bold line face in Figure 7), oblique to depositional strike. The 12 numbered trough cross-bed sets were chosen to define best fit elliptical curves (cf. Figure 4). B) Interpretation of the photomontage. Trough (gray) and tabular (yellow) cross-beds are numbered sequentially and interpreted to be stacked vertically within a tidal bar deposit. Note that the numbering starts at 10, as nine underlying cross-bed sets are exposed on the adjacent SSW-NNE-oriented face (dotted line face in Figure 7).

Figure 9: Distribution of A) the preserved height H_A and B) preserved apparent width W_A of 49 trough cross-bed sets exposed on the WNW-ESE-oriented face of Gecko Nose (bold line face in Figure 7; Figure 8 B), oblique to depositional strike. A log-normal distribution of the form LogN(μ,σ^2) is interpreted, with parameters μ: mean value; σ: standard deviation. p corresponds to the Kolmogorov-Smirnov test criterion: a value of 1 corresponds to a perfect fit of the data with a log-normal distribution. For the height H_A in A), μ = 0.3 cm and σ = 0.4 cm with p = 0.82; for the width W_A in B), μ = 3.1 cm and σ = 1.4 cm with p = 0.98.

Figure 10: Point clouds defining the 90 foreset-toeset surfaces traced from three cross-bed sets of the WNW-ESE-oriented face of Gecko Nose (numbered 34, 50 and 52 in Figure 8 A). The surfaces are translated so that their foreset-to-toeset junction points (labelled *O* in Figure 5) are superimposed, and a best-fit line for a foreset-toeset template surface is determined (bold line). This line is described by equation (5) with the curvature parameter A = 5.5×10^{-3}, and the resulting line has a very strong correlation to the data (R^2 = 0.98).

Figure 11: Distribution of foreset thickness F_T for the 544 foreset-toeset surfaces of 12 studied cross-bed sets (Figure 8 A). A log-normal distribution of the form LogN(μ,σ^2) is interpreted with parameters μ, mean value = 5.9 cm; σ, standard deviation = 2.0 cm.

Figure 12: Point cloud defining the coverage of mudstone drapes along 90 foreset-toeset surfaces traced from three cross-bed sets (numbered 34, 50 and 52 in Figure 8 A). A best-fit line for mudstone drape coverage along a foreset-toeset surface is determined (bold line). This line is described by equation (4) with parameters M = -1.004, N = -4.316, and O = 1.610, and it correlates very strongly to the data (R^2 = 0.99).

Figure 13: A) 3D view of the generic trough cross-bedding model, generated with input parameters extracted from the Gecko Nose outcrop and summarized in Table 1. Only mudstone drapes are displayed here and sandstone is removed from the model. The model displays a mudstone drape coverage of 25% along the foreset parts, and a coverage of 57 % along the toeset parts of the foreset-toeset surfaces. The trough aspect of the cross-bedding appears in the strike direction. Warm colors indicate increasing height of mudstone drapes above the cross-bed base, for each cross-bed set. B) Orthogonal sections through the same model with mudstone and sandstone layers colored in black and yellow respectively. The layers of mudstone have a constant thickness of 3.5 mm in the whole model. C) Dip-oriented cross-section of the model presented in part A representing the cross-bedding surfaces. D) The same dip-oriented cross-section but with the 25% mudstone drape coverage of foresets and 57% mudstone drape coverage of toesets.

Figure 14: A) 3D view of the generic tabular cross-bedding model, generated with input parameters extracted from the Butterfly canyon outcrop and summarized in Table 1. Only mudstone drapes are displayed here and sandstone is removed from the model. The model displays a mudstone drape coverage of 25% along the foreset parts, and a coverage of 57 % along the toeset parts of the foreset-toeset surfaces. B) Orthogonal sections through the model. The layers of mudstone have a constant thickness of 3.5 mm in the whole model. C) Dip-oriented cross-section of the model presented in part A representing the cross-bedding surfaces. D) The same dip-oriented cross-section but with the 25% mudstone drape coverage of foresets and 57% mudstone drape coverage of toesets. Same color schemes than in Figure 13.

Figure 15: Comparison between outcrop photographs (top row), and corresponding cross-sections of the surface-based models showing foreset-toeset surfaces (central row) and mudstone drapes along these surfaces (bottom row). Column A) shows dip-oriented sections from the Butterfly Canyon outcrop and model. Column B) shows strike-oriented sections from the Gecko Nose outcrop and model (red rectangle in Figure 8 A).

Figure 16: Determination of effective permeability from the flow simulation results of the two outcrop models (Figures 13, 14). If the studied heterolithic sandstone features trough cross-bedding with muddy toeset regions, the Gecko Nose model should be used for reference; if the studied heterolithic sandstone features tabular cross-bedding with a predominance of sandy foreset regions, the Butterfly Canyon model should be used. The two examples of effective permeability derivation presented in the text are featured with

straight vertical lines: k_{sand} = 500 md and k_{sand} = 100 md. The resulting effective permeability k_e can be read at the intersection of these straight lines with the different curves.

Table captions

Table 1: Input parameters for the Gecko Nose and Butterfly Canyon models (Figures 13, 14).

Table 2: Results for the Gecko Nose and Butterfly Canyon models (Figures 13, 14) after single phase flow simulation. All measurements are dimensionless.

Table 1:

Input parameter	Symbol	Unit	Trough cross-bedded model (Gecko Nose)	Tabular cross-bedded model (Butterfly Canyon)	Definition
Volume of the model	V_T	m^3	9	9	
Elemental volume length	L_E	m	20	20	Trough cross-beds are modelled as highly elongate, oblate ellipsoids with $L_E >> W_E > H_E$. Tabular cross-beds are modelled as oblate ellipsoids with $W_E \geq L_E > H_E$, which yields laterally continuous sheets at the model scale (geometrical mean value $E[W_E]$ ± standard deviation $\sigma[W_E]$).
Elemental volume width	W_E	m	4.85 ± 1.67	20	
Elemental volume height	H_E	m	1.35 ± 0.55	1.35 ± 0.55	
Preserved length of elemental volume	L_A	m	80% of L_E	100% of L_E	These parameters define the preserved aspect of the ellipsoidal elemental volumes in the model, after erosion at the base of overlying elemental volumes (geometrical mean value $E[W_A]$ ± standard deviation $\sigma[W_A]$).
Preserved width of elemental volume	W_A	m	50% of W_E	100% of W_E	
Preserved height of elemental volume	H_A	m	30% of H_E	40% of H_E	
Elemental volume density	D	m^{-3}	6 elemental volumes in 9 m^3	4 elemental volumes in 9 m^3	Number of ellipsoidal elemental volumes present per unit volume of the model.
Elemental volume orientation	ϑ	°	0	0	The azimuthal orientation angle ϑ of the ellipsoidal elemental volumes corresponds to the paleocurrent direction indicated by the foreset-toeset surfaces within a cross-bed set.
Number of cross-bedding surfaces	N_{CB}	-	≈500	≈170	
Parabolic curvature of foreset-toeset template surfaces	A	-	5.5×10^{-3}	5.5×10^{-3}	Characteristic coefficient of the square term for a parabolic curve, $z(x) = Ax^2$ as equation (1)

Foreset thickness	F_T	cm	5.85 ± 3.88	10 ± 3.88	Distance between two consecutive foreset-toeset surfaces, measured between their junction points *O* and *O’* (Figure 5).
Toeset dip angle	α	°	8	1	Angle between the straight toeset surface and the median reference plane of the ellipsoidal elementary volume Γ (Figure 5)
Angle of dune climb	δ	°	5	0	Angle between the median reference plane Γ and the boundary surface Δ which separates the foreset and the toeset parts in an elementary volume (Figure 5)
Foreset to toeset volume ratio	$R_{F/T}$	-	6.5 : 1	24 : 1	Ratio of the volume occupied by foreset by the volume occupied by toeset in the model
Mudstone frequency function	$f(M,N,O)$	-	Function f of Figure 12	Function f of Figure 12	Defined in 2D, along the azimuth of the ellipsoidal elemental volume (i.e. dip direction), according to the distance from the top of the foreset to the junction point *O* with the toeset. M = -1.004, N = -4.316, and O = 1.610 in equation (7)
Mudstone drape coverage	M_C	-	Foreset 25% Toeset 57%	Foreset 25% Toeset 57%	Mudstone patches are added along the foreset-toeset template surfaces until a specific proportion M_C of their area is covered. $M_C = A_M / A_F$
Total area of the preserved foreset-toeset surface	A_F	cm^2	-	-	
Area of the foreset-toeset surface covered by mudstone	A_M	cm^2	-	-	
Mudstone patch length	MP_L	cm	[0 – 20] Uniform distribution	[0 – 100] Uniform distribution	After the dimension of the major axis of the elliptical patch MP_L is defined, the dimension of the minor axis MP_W is randomly set as a fraction of MP_L
Mudstone patch width	MP_W	cm	[0 – 20] Uniform distribution Smaller than MP_L	[0 – 20] Uniform distribution Smaller than MP_L	

Table 2:

Measured parameter	Symbol	Trough cross-bedded model (Gecko Nose)	Tabular cross-bedded model (Butterfly Canyon)
Mudstone volume fraction	V_M/V_T	0.11	0.06
Sandstone volume fraction	V_S/V_T	0.89	0.94
Normalized effective dip horizontal permeability	k_d	47.5%	70.0%
Normalized effective strike horizontal permeability	k_s	72.8%	90.0%
Normalized effective vertical permeability	k_v	2.4%	2%
Ratio of vertical permeability by horizontal permeability	k_v/k_h	0.0399	0.0025

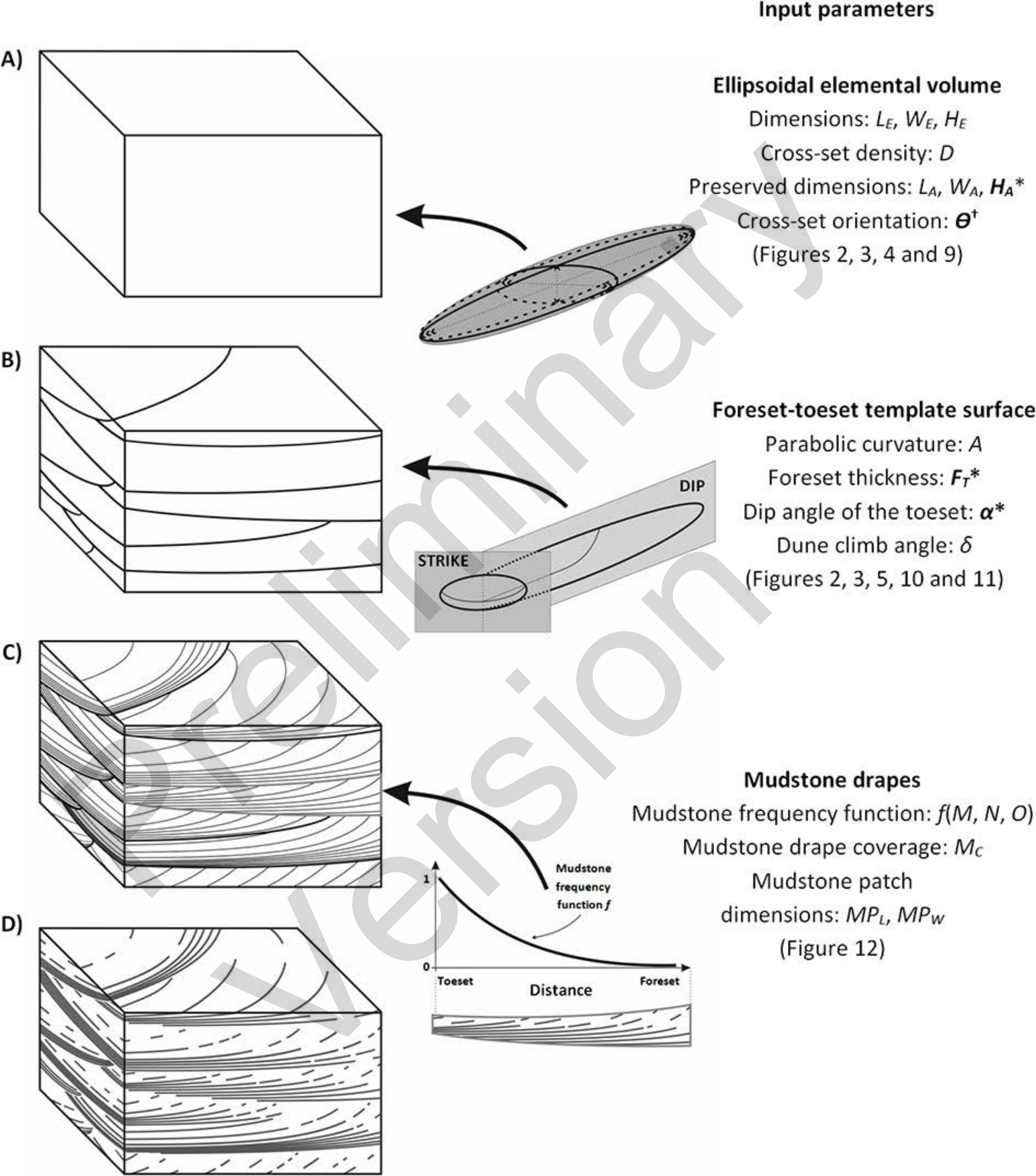
Input parameters
A)
Ellipsoidal elemental volume
Dimensions: L_E, W_E, H_E
Cross-set density: D
Preserved dimensions: L_A, W_A, $\boldsymbol{H_A}$*
Cross-set orientation: $\boldsymbol{\Theta}^{\dagger}$
(Figures 2, 3, 4 and 9)
B)
STRIKE
DIP
Foreset-toeset template surface
Parabolic curvature: A
Foreset thickness: $\boldsymbol{F_T}$*
Dip angle of the toeset: $\boldsymbol{\alpha}$*
Dune climb angle: δ
(Figures 2, 3, 5, 10 and 11)
C)
Mudstone drapes
Mudstone frequency function: $f(M, N, O)$
Mudstone drape coverage: M_C
Mudstone patch
dimensions: MP_L, MP_W
(Figure 12)
Mudstone
frequency
function f
1
0
Toeset
Distance
Foreset
D)

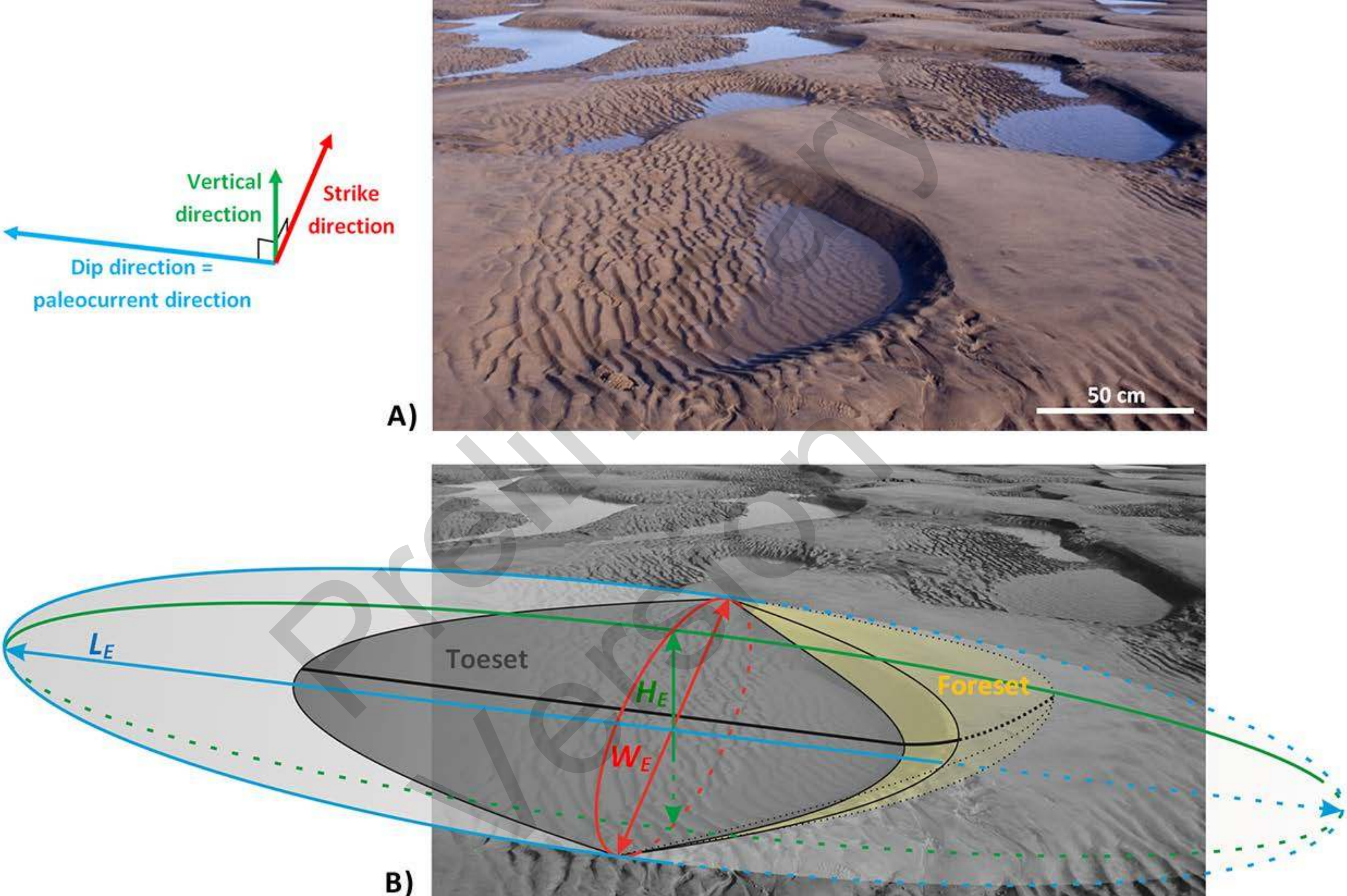
Vertical
direction
Strike
direction
Dip direction =
paleocurrent direction
A)
50 cm
L_E
Toeset
H_E
W_E
Foreset
B)

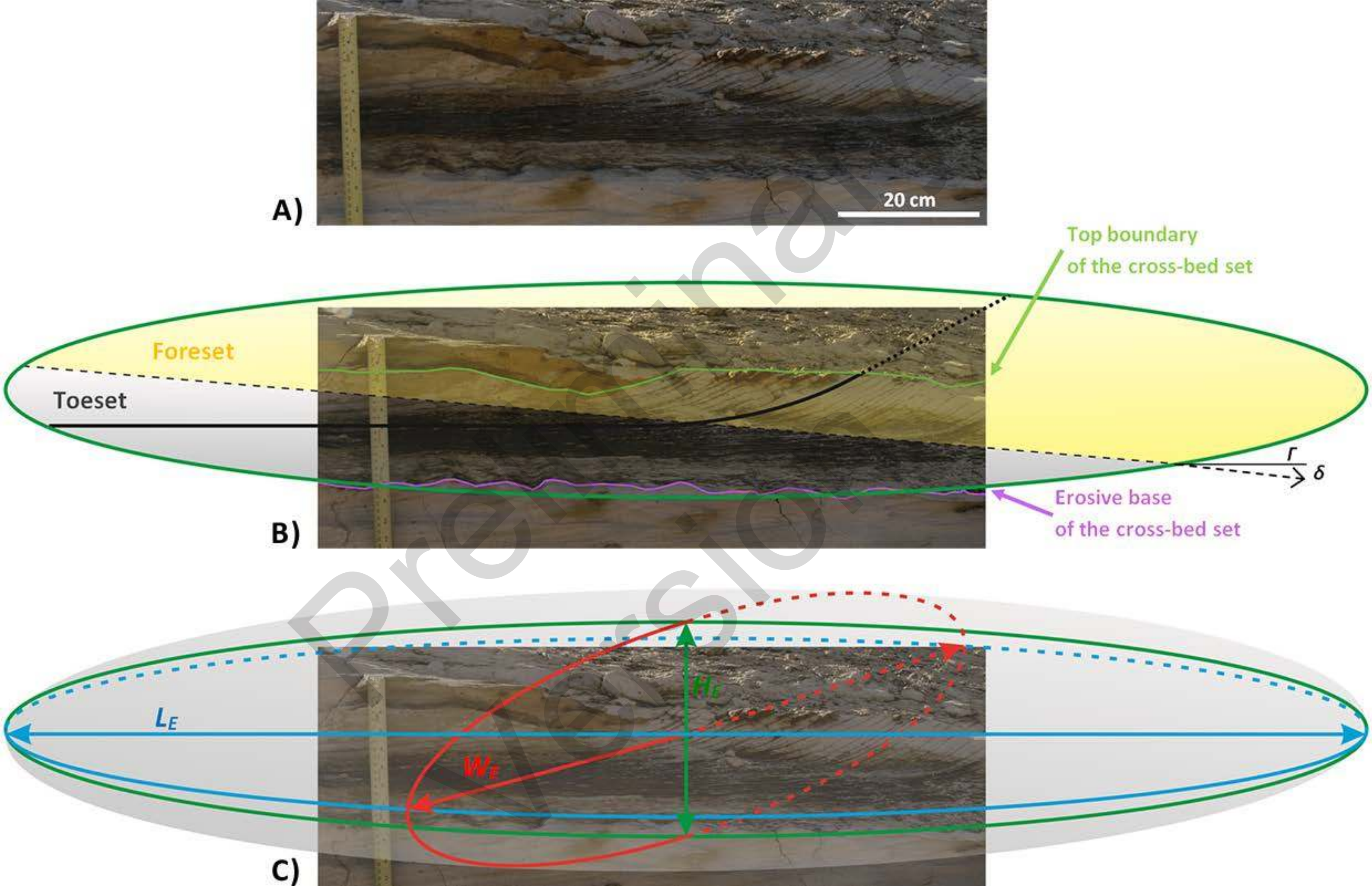

A)
20 cm
B)
Foreset
Toeset
Top boundary
of the cross-bed set
Erosive base
of the cross-bed set
Γ
δ
C)
L_E
H_E
W_E

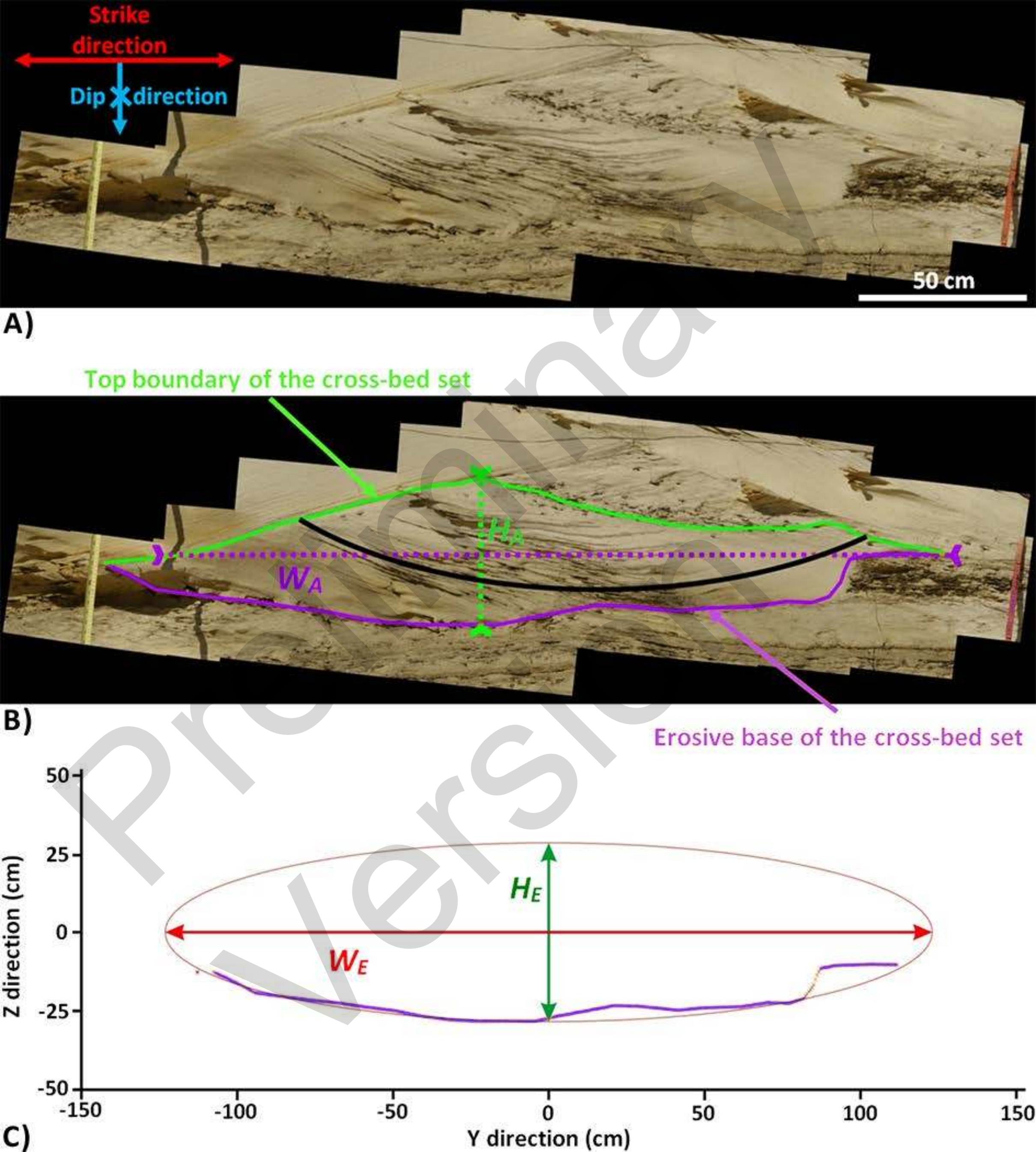
Strike direction
Dip direction
50 cm
A)
Top boundary of the cross-bed set
H_A
W_A
B)
Erosive base of the cross-bed set
H_E
W_E
Z direction (cm)
Y direction (cm)
50
25
0
-25
-50
-150
-100
-50
0
50
100
150
C)

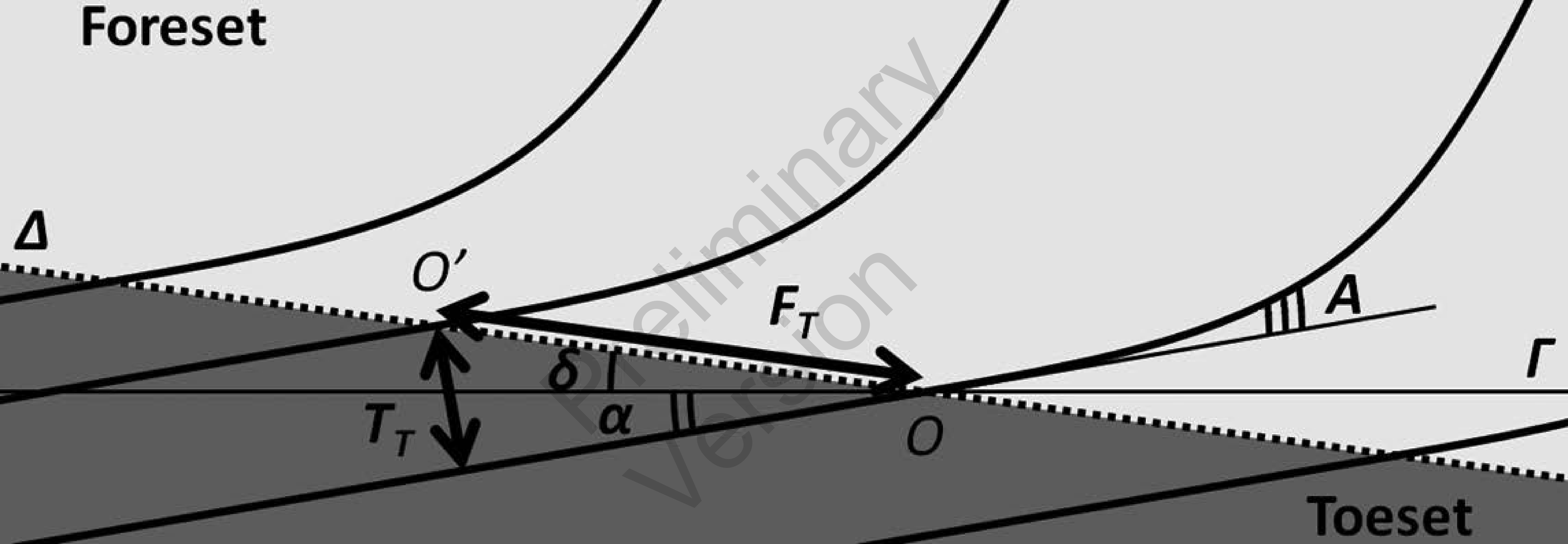

Foreset
Δ
O′
F_T
A
Γ
δ
α
T_T
O
Toeset

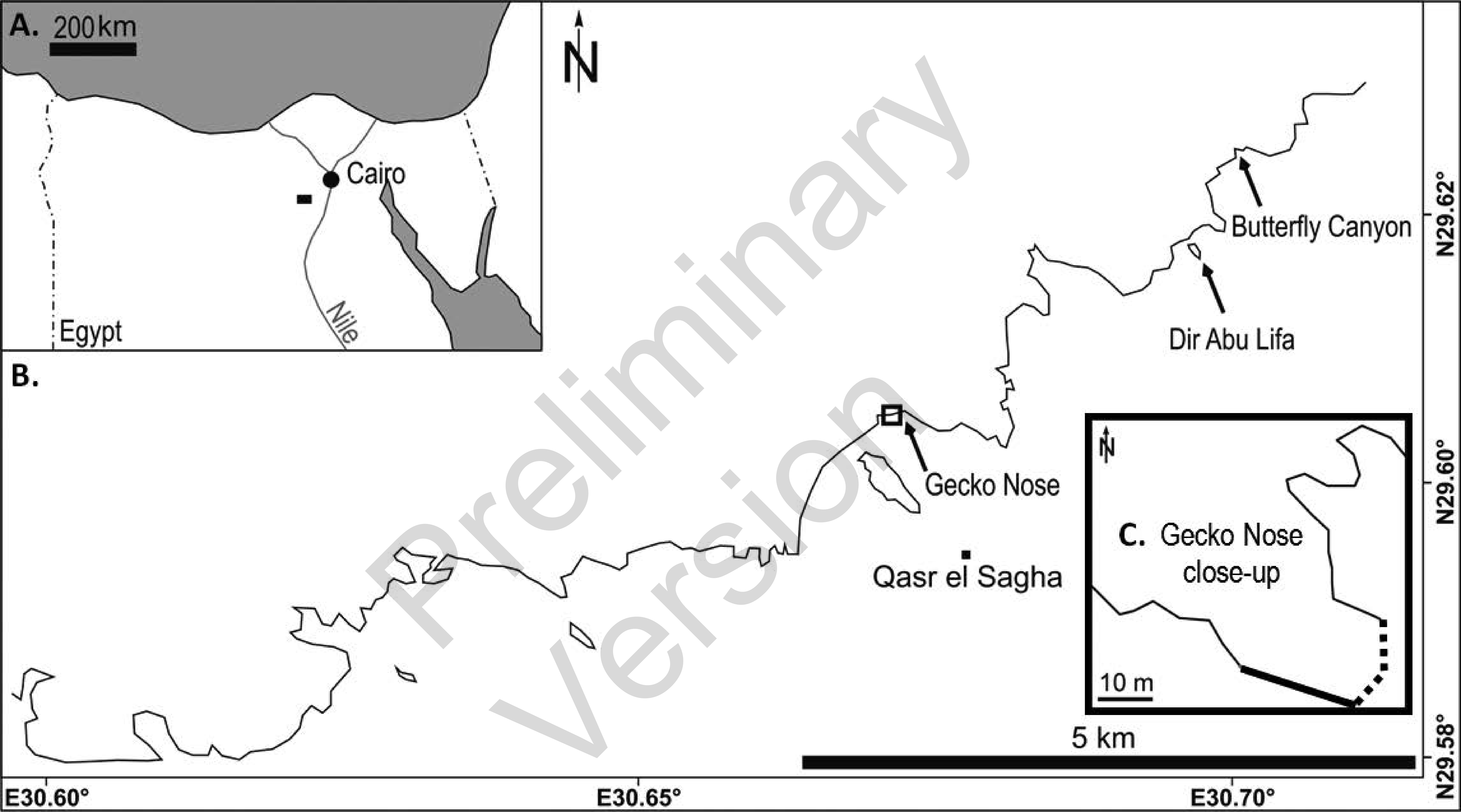
A.
200 km
Cairo
Nile
Egypt
B.
N
Butterfly Canyon
Dir Abu Lifa
Gecko Nose
Qasr el Sagha
C. Gecko Nose close-up
N
10 m
5 km
N29.62°
N29.60°
N29.58°
E30.60°
E30.65°
E30.70°


N = 196
N110|N210
0.0
N290
-17.0m
3.0m
N030
12.5m

A)

B)

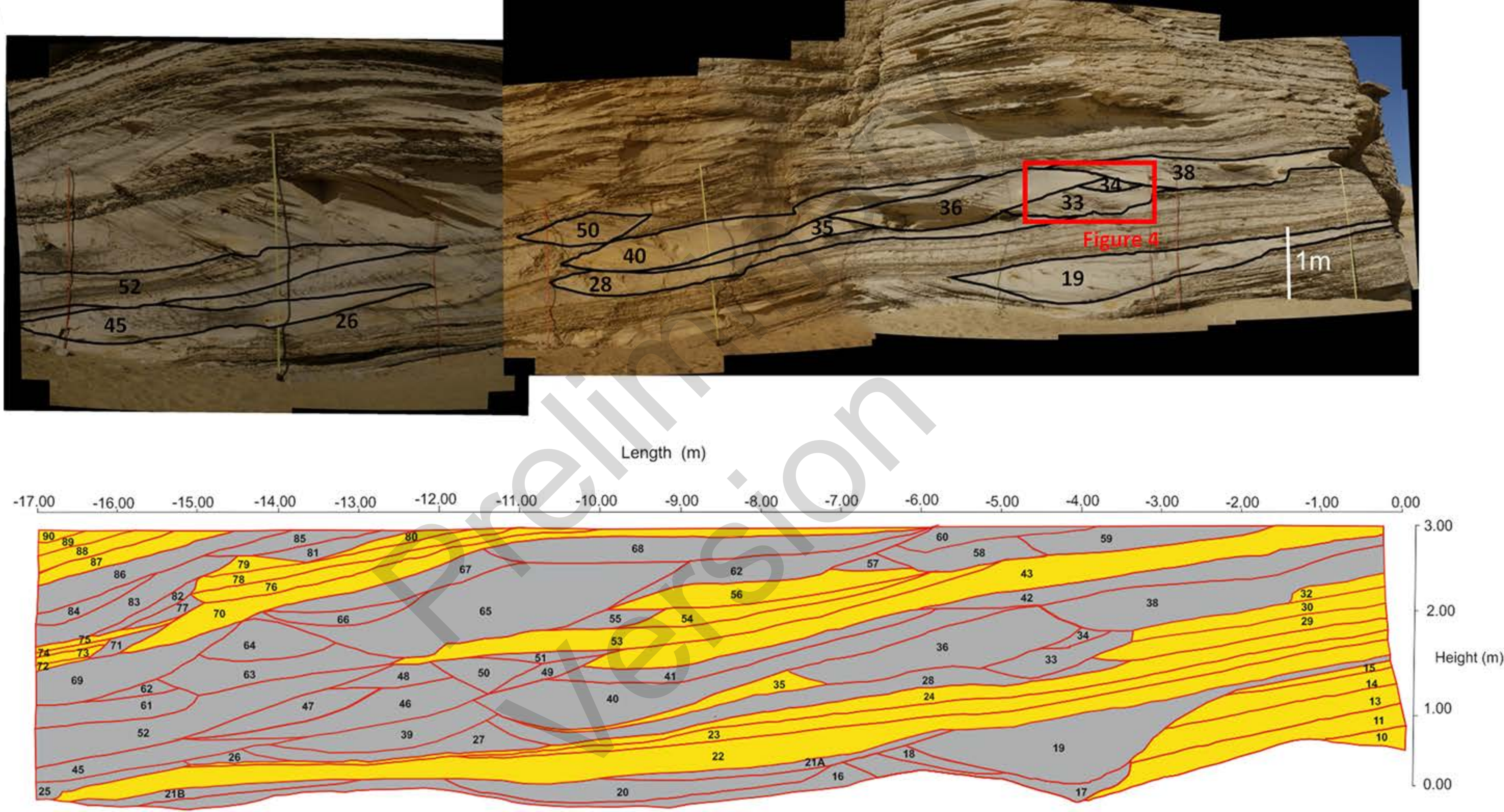
52
45
26
50
40
28
35
36
33
34
38
19
Figure 4
1m
Length (m)
-17.00
-16.00
-15.00
-14.00
-13.00
-12.00
-11.00
-10.00
-9.00
-8.00
-7.00
-6.00
-5.00
-4.00
-3.00
-2.00
-1.00
0.00
Height (m)
3.00
2.00
1.00
0.00
90
89
88
87
86
85
81
80
79
78
76
68
67
60
59
58
57
62
56
43
42
32
30
29
38
84
83
82
77
70
66
65
55
54
53
36
34
33
75
74
73
72
71
64
51
49
41
28
24
15
14
13
11
10
69
63
62
61
48
50
40
35
47
46
52
39
27
23
22
21A
18
19
45
26
25
21B
20
16
17

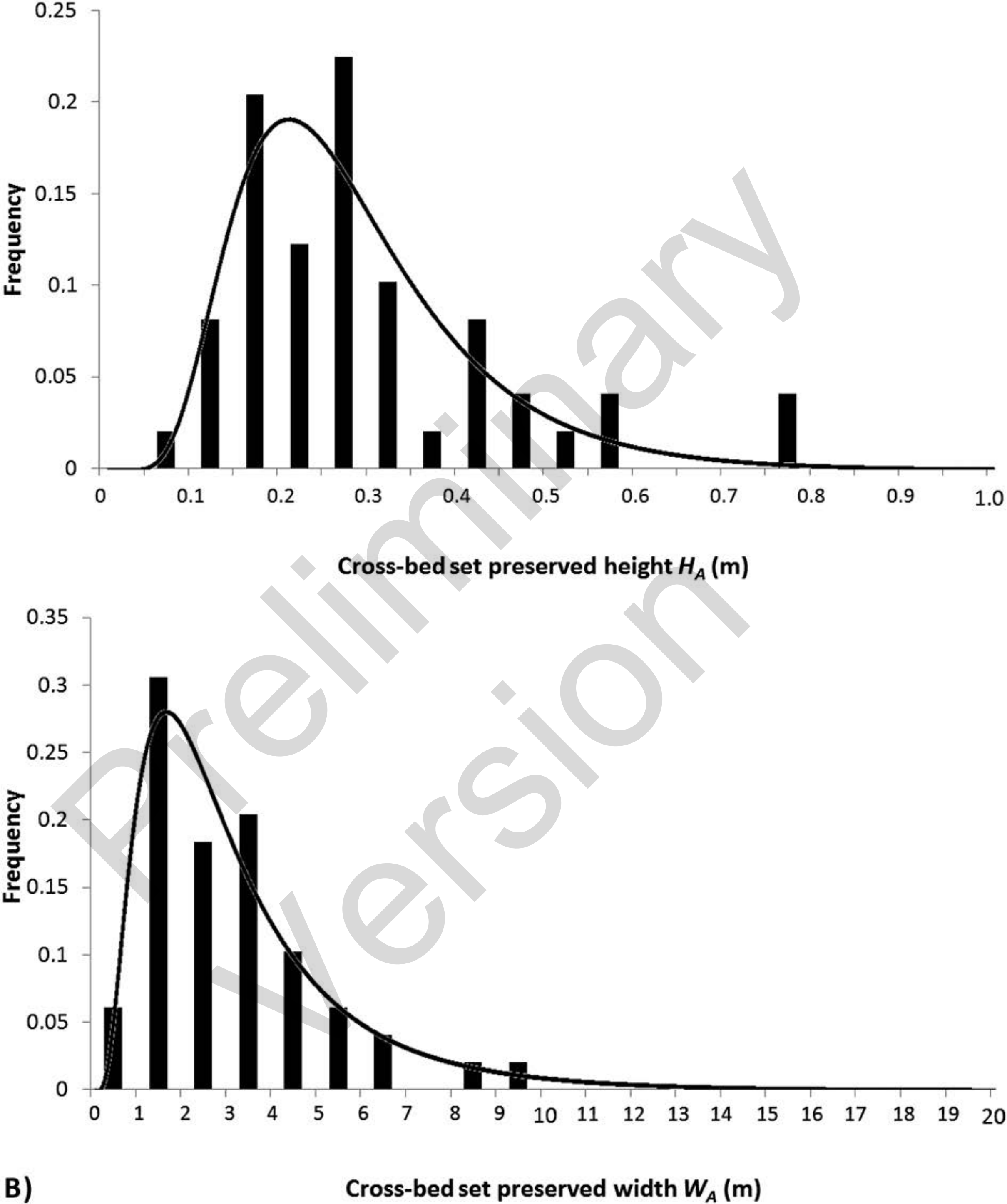
Frequency
0.25
0.2
0.15
0.1
0.05
0
0 0.1 0.2 0.3 0.4 0.5 0.6 0.7 0.8 0.9 1.0
Cross-bed set preserved height H_A (m)
Frequency
0.35
0.3
0.25
0.2
0.15
0.1
0.05
0
0 1 2 3 4 5 6 7 8 9 10 11 12 13 14 15 16 17 18 19 20
B)
Cross-bed set preserved width W_A (m)

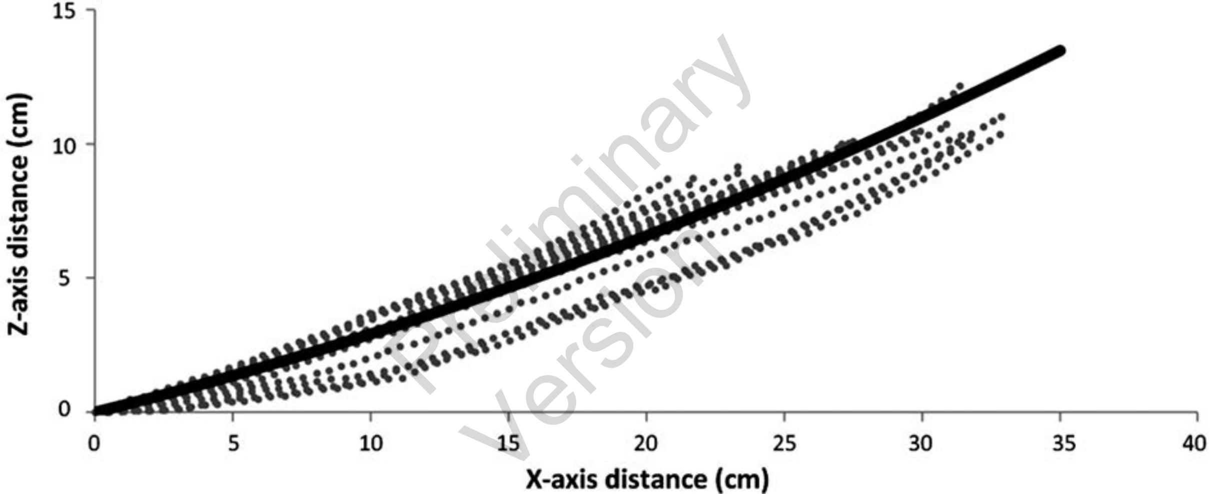

15
10
5
0
Z-axis distance (cm)
0
5
10
15
20
25
30
35
40
X-axis distance (cm)
Preliminary
Version

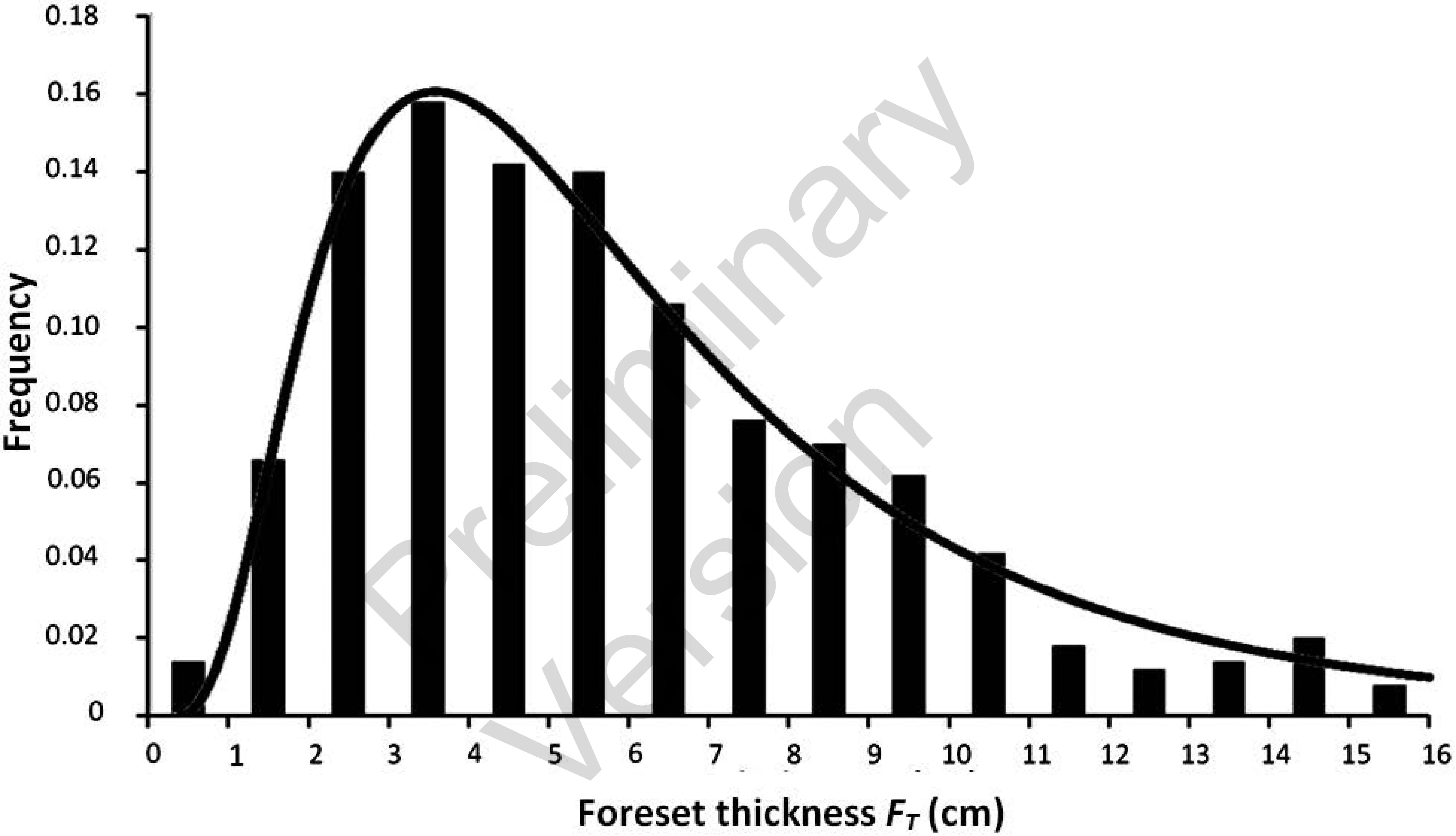

0.18
0.16
0.14
0.12
0.10
0.08
0.06
0.04
0.02
0
Frequency
0 1 2 3 4 5 6 7 8 9 10 11 12 13 14 15 16
Foreset thickness F_T (cm)
Preliminary Version

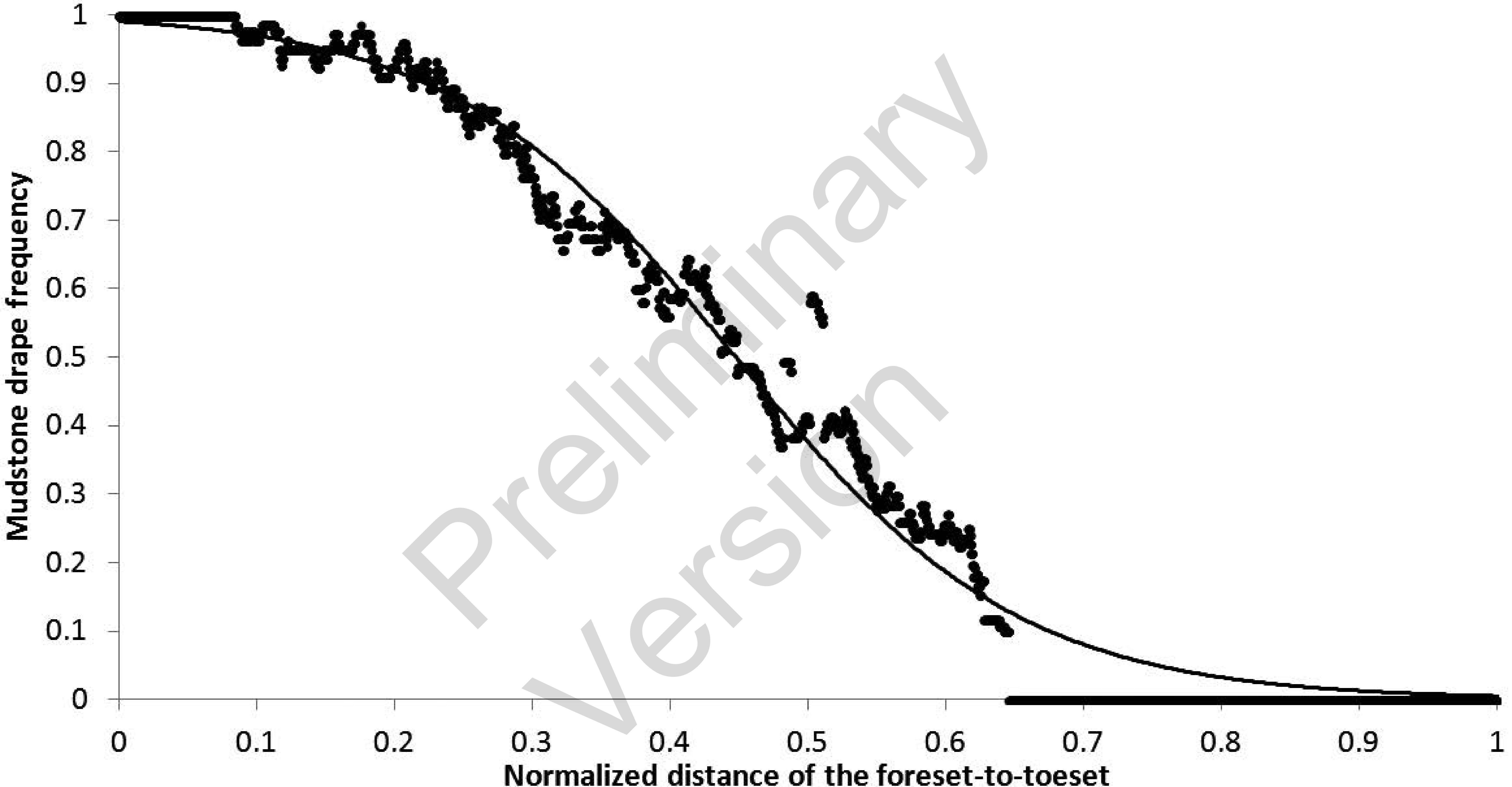

Mudstone drape frequency
1
0.9
0.8
0.7
0.6
0.5
0.4
0.3
0.2
0.1
0
0
0.1
0.2
0.3
0.4
0.5
0.6
0.7
0.8
0.9
1
Normalized distance of the foreset-to-toeset
Preliminary Version

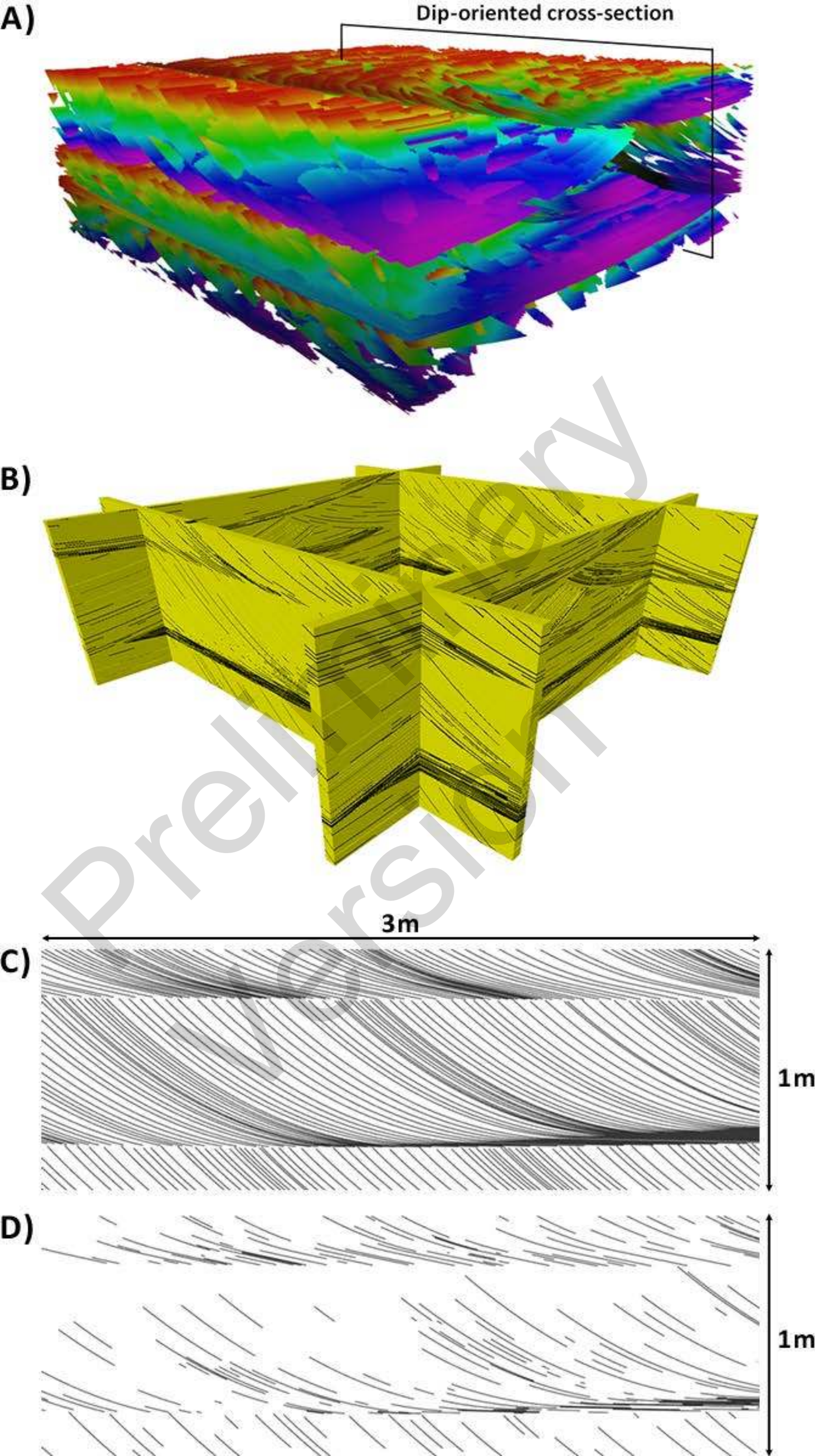
A)
Dip-oriented cross-section
B)
3m
C)
1m
D)
1m

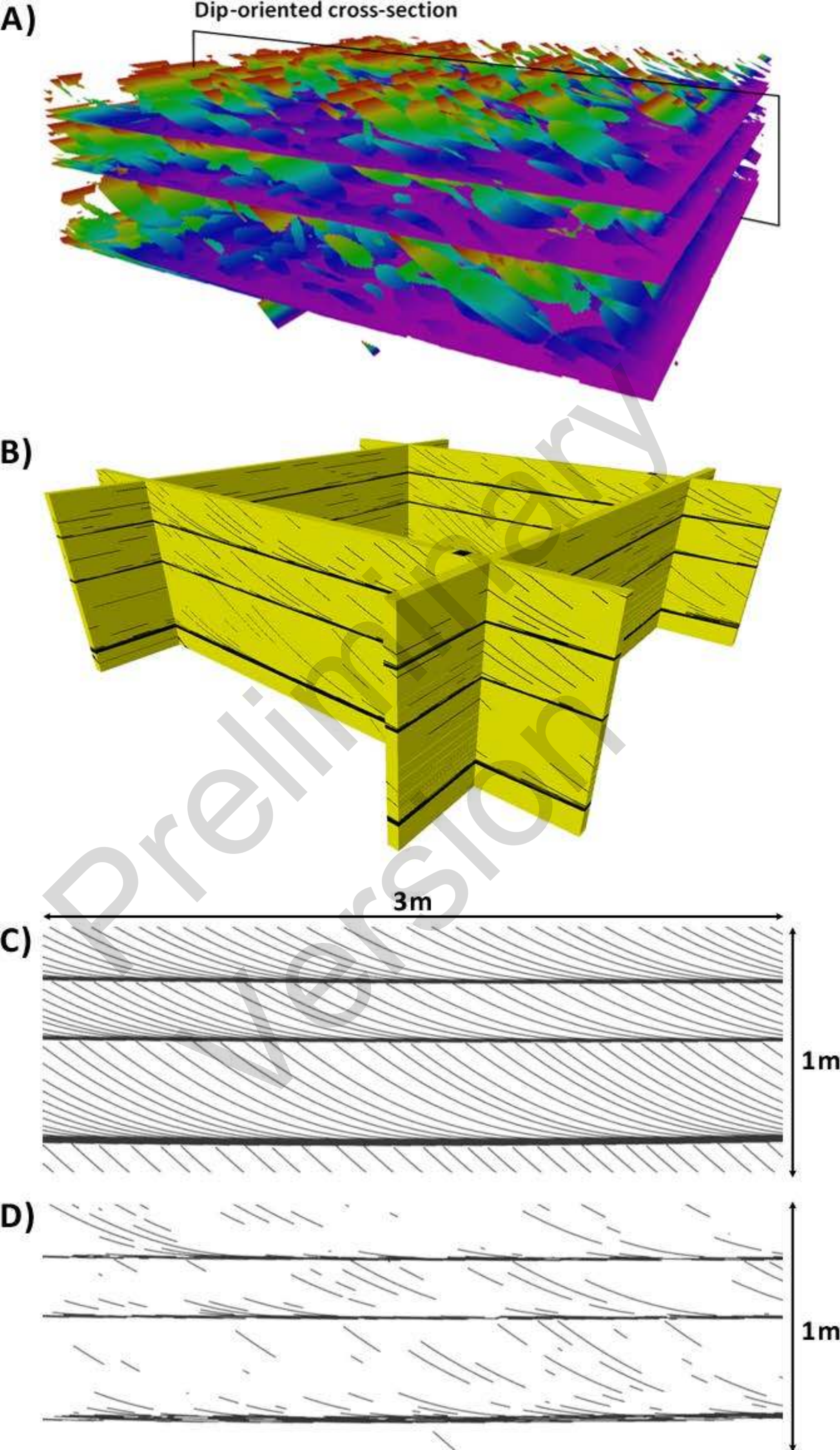
A)
Dip-oriented cross-section
B)
3m
C)
1m
D)
1m

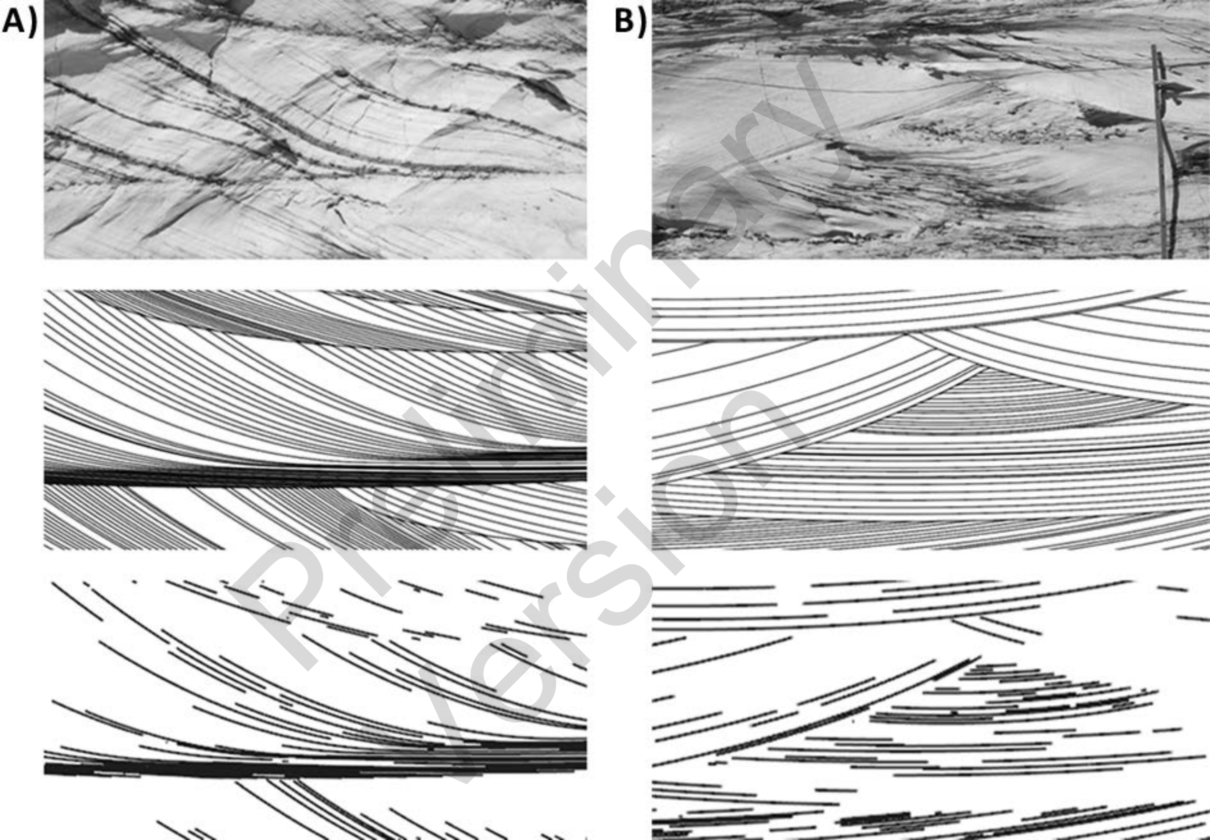
A)
B)

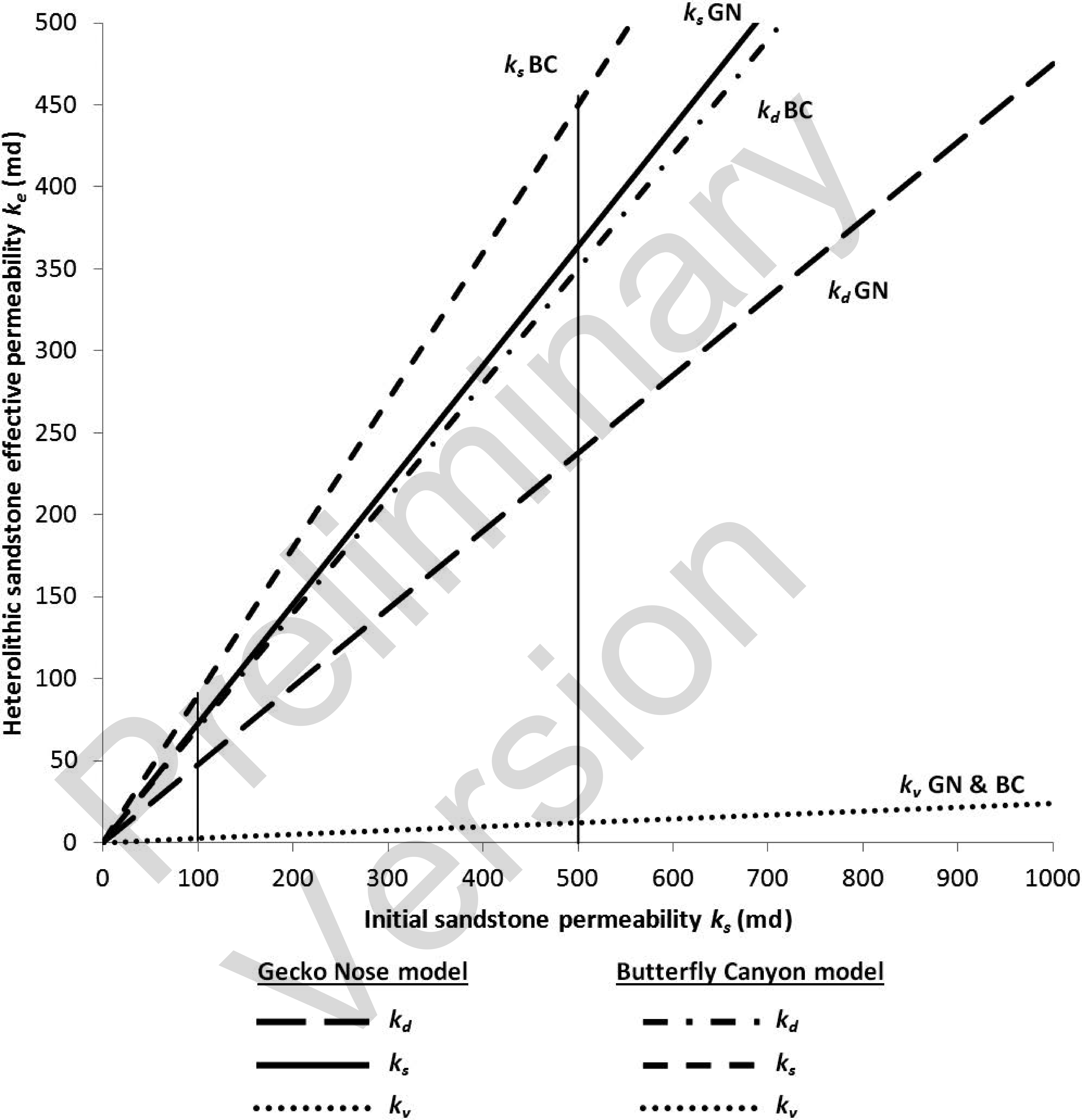

500
450
400
350
300
250
200
150
100
50
0
0
100
200
300
400
500
600
700
800
900
1000
Heterolithic sandstone effective permeability k_e (md)
Initial sandstone permeability k_s (md)
k_s GN
k_s BC
k_d BC
k_d GN
k_v GN & BC
Gecko Nose model
k_d
k_s
k_v
Butterfly Canyon model
k_d
k_s
k_v